University of Tartu

Faculty of Science and Technology

Institute of Chemistry

Miriam Koppel

The mobility of H_2 Adsorbed in Mo_2C Derived Carbon Materials with Different Porous Structures Studied with Quasi-Elastic Neutron Scattering

Master's Thesis (30 ECTS)

Materials Science and Technology

Supervisors: Riinu Härmas, M. Sc

Rasmus Palm, Ph. D

Tartu 2021

Adsorbeerunud H_2 liikuvuse uurimine erinevate poorsete struktuuridega Mo_2C-st sünteesitud süsinikmaterjalides kvaasielastse neutronhajumise meetodiga

H_2 on huvipakkuv alternatiiv fossiilsetele kütustele, sest H_2 oksüdeerumisel ei eraldu saasteaineid. H_2 kasutuselevõtu puhul on peamiseks probleemiks selle transport ja hoiustamine. Üks võimalik lahendus H_2 hoiustamiseks on füüsikaline adsorptsioon poorsetes süsinikmaterjalides. Karbiididest sünteesitud süsinikmaterjalid on head mudelmaterjalid uurimaks poorsuse mõju vesiniku hoiustamise võimele. Kolme Mo_2C-st sünteesitud süsinikmaterjali (sünteesitud temperatuuridel 700 ºC, 800 ºC ja 900 ºC ja edaspidi nimetatud C700, C800 ja C900) poorne struktuur määrati N_2, Ar, CO_2 ja H_2 adsorptsiooni meetodil. Tulemuseks saadi, et sünteesitemperatuuri suurenedes materjalide eripind ja pooriruumala vähenevad. Mitme gaasiga adsorptsiooni mõõtmise eeliseks on see, et võimalik on usaldusväärselt määrata materjalide poorne struktuur laias pooride vahemikus, mille tulemusena saab uurida H_2 liikuvust ultramikropoorides (poori laius < 7 Å), mikropooridest (7 < poori laius < 20 Å) ja mesopoorides (poori laius > 20 Å).

Adsorbeerunud H_2 liikuvust (difusiooni) uuriti kvaasielastse neutronhajumise meetodil kolmel laadimisrõhul ja kuuel temperatuuril. Järeldati, et madalamal laadimisrõhul oli H_2 adsorbeerunud eelkõige ultramikropoorides, keskmisel laadimisrõhul oli H_2 adsorbeerunud eelkõige ultramikro- ja mikropoorides ning kõrgemal laadimisrõhul oli H_2 adsorbeerunud kõikides poorides. Tulemuseks saadi, et temperatuuri kasvades H_2 liikuvus suureneb ning H_2 desorbeerub. Madalal temperatuuril (50 K) on H_2 liikuvus C700 ja C800 ultramikropoorides väga piiratud. Kui ultramikropooride ruumala väheneb, siis H_2 muutub liikuvamaks. Keskmisel ning kõrgemal rõhul oli näha H_2 liikumist kahes erinevas kiiruste piirkonnas, mida uuritakse põhjalikumalt edasi. Difusiooniprotsessi aktivatsioonienergiatest järeldati, et mikropoorid lisaks ultramikroporidele aitavad piirata H_2 liikuvust, aga mesopooride võimekus H_2 kinni hoida on väiksem.

Märksõnad: vesiniku hoiustamine, karbiidset päritolu süsinik, gaasi adsorptsioon, kvaasi-elastne neutronhajumine

CERCS code: P400 Füüsikaline keemia

The Mobility of H_2 Adsorbed in Mo_2C Derived Carbon Materials with Different Porous Structures Studied with Quasi-Elastic Neutron Scattering

H_2 is a promising energy vector since the oxidation of H_2 produces no pollutants. However, the current methods for transportation and storage of H_2 are not very efficient. One method for storing H_2 is physical adsorption on porous carbon adsorbent. Carbide derived carbons are good model materials for investigating the influence of porosity on the H_2 storage. The porous structure of three Mo_2C derived carbon materials synthesized at 700 ºC, 800 ºC and 900 ºC (denoted as C700, C800 and C900) has been characterized with N_2, Ar, CO_2 and H_2 adsorption methods. From these results, it was concluded that as the synthesis temperature of the carbide increases, the pore volume and specific surface area decrease. Accurate confirming the pore volumes of the samples enables to investigate how the porous structure influences the mobility of H_2 adsorbed in the ultramicropores (width < 7 Å), micropores (7 < width < 20 Å) and mesopores (width > 20 Å) of the samples.

The mobility (diffusion) of H_2 adsorbed in the samples was investigated with quasi-elastic neutron scattering method at three different H_2 loading pressures and at six different temperatures. At the lowest H_2 loading pressure, H_2 was mostly adsorbed in the ultramicropores of the samples. At moderate loading pressure, H_2 was mostly adsorbed in the ultramicro- and micropores of the samples and at the highest loading pressure, H_2 was adsorbed in all of the available pores. As the temperature increases, the diffusion coefficients (D) also increase, showing that the heat fluctuations initiate the faster motion and desorption of H_2 molecules. When H_2 was adsorbed mostly in ultramicropores, the small D values of H_2 adsorbed in C700 and C800 at 50 K indicates a strong confinement of H_2. When the ultramicropore volume decreases, H_2 becomes more mobile. At moderate and high loading pressure, H_2 diffusion in two timescales is observed and will be investigated more thoroughly in the future. The activation energies of the diffusion process indicate that micropores, in addition to ultramicropores help to confine H_2, but mesopores do not have noticable effect on the H_2 confinement.

Keywords: hydrogen storage, carbide-derived carbons, gas adsorption, quasi-elastic neutron scattering

CERCS code: P400 Physical chemistry

Contents

Abbreviations

2D-NLDFT-HS – Two-Dimensional Non-Local Density Functional Theory for Heterogeneous Surface

ASAP 2020 – Accelerated Surface Area and Porosity System

BET – Brunauer-Emmett-Teller

CDC – Carbide-derived carbon

DOE – U.S. Department of Energy

EL – Elastic component

FWHM – Full width at half maximum

HWHM – Half width at half maximum

QENS – Quasi-elastic neutron scattering

QE – Quasi-elastic component, where QE1 and QE2 are slower (narrower) and faster (broader) components, respectively

ND – Neutron diffraction

SAIEUS – Solution of Adsorption Integral Equation Using Splines

SANS – Small-angle neutron scattering

STP – Standard temperature and pressure (0 ℃ and 1 bar)

Introduction

The future energy demand is expected to increase significantly because of the increasing world population and quick economic development. However, due to the rising demand for better air quality and concern over climate change, it is crucial to introduce more renewable energy to meet the increasing energy demand. One of the greatest obstacles to the widespread use of renewables is the lack of efficient energy storage methods. H_2 is a potential energy storage medium not only because it can be produced from renewable sources, but because it has the highest energy content per unit mass of any fuel. The energy content of H_2 is 120 MJ kg^{-1} (lower heating value). In contrast, gasoline's energy content is 44 MJ kg^{-1} (lower heating value), approximately three times lower than that for H_2. However, on a volume basis, the situation is reversed: 8 MJ kg^{-1} for liquid H_2 versus 31 MJ kg^{-1} for liquid gasoline (lower heating value), thus approximately four times higher than for H_2. The low volumetric density is the main obstacle to H_2 storage in mobile applications [1,3].

H_2 occupies more volume than an equal mass of gasoline at STP (standard temperature and pressure), so either very large containers, high pressures (350–700 bar) and/or very low temperatures (H_2 liquifies at 20 K) are needed to store a reasonable amount of H_2 [3]. The ultimate target of H_2 storing density of 50 g dm^{-3} has been set by DOE [2]. However, H_2 being a light gas (density 0.09 g dm^{-3} at STP) and diffusive in air (diffusion coefficient 0.61 cm^2 s^{-1} in air at STP) is difficult to store [3]. H_2 storage density of 40 g dm^{-3} at 700 bar does not reach the density goals for on-board storage set by DOE [4]. Physical adsorption of H_2 on a high surface area and microporous material could be a potential solution for these problems because it is fast, energy-efficient, and H_2 can be stored at reasonable pressure and temperature and with higher density than gaseous H_2 at low pressures [3,6]. H_2 density of 43.2 g dm^{-3} has been reported at 77 K and 20 bar [5].

High surface area and microporosity are crucial for H_2 storage [6]. Carbide-derived carbons (CDCs) are materials with well-tunable porosity characteristics, which can be influenced by choosing the precursor carbide and controlling the synthesis conditions. This enables to synthesize carbon materials with a wide range of both micro- and mesopore volume, which makes CDCs excellent model materials to study the influence of porous structure on H_2 storage [7].

Three carbon materials synthesized from Mo_2C at temperatures ranging from 700 ℃ to 900 ℃ (denoted as C700, C800 and C900) were characterized with the gas adsorption analysis method, using different gases. The surface areas, pore volumes and pore size distributions were determined. These materials have previously been investigated with several neutron scattering methods such as small angle neutron scattering (SANS) [8], neutron diffraction (ND) [10] and with quasi-elastic neutron scattering (QENS) [9]. However, the in-depth analysis of the QENS data for C700−C900 has not been previously done. The SANS data revealed that as the synthesis temperature of the CDCs increases, the shape of the pores changes from cylindrical to slit-like geometry [8].

QENS method was used to investigate the impact of surface area and pore volume in different ranges and pore size distributions on the mobility (diffusion) of H_2. Parameters describing the diffusion process have been calculated and compared with the porosity characteristics of the three materials. In this manner, a detailed understanding of the effect of the porous structure of carbon on the confinement of H_2 molecules has been achieved, which is essential for tuning the porosity characteristics of the carbon adsorbent and, therefore, maximizing the H_2 adsorption capacity and energy efficiency of the H_2 storage systems.

1. Literature overview

1.1 H_2 storage in microporous carbons

The H_2 storage properties of high surface area carbon materials have been extensively studied because of their chemical stability and relatively low density. In addition to the surface area, also the volume of ultramicropores (pore width $w < 0.7$ Å), micropores ($0.7 < w < 20$ Å) and mesopores ($20 < w < 500$ Å) have a crucial role in the H_2 storage and confinement capability of a porous carbon [11]. Since the interaction between the adsorbent and H_2 molecule is weak, and H_2 is easily released when the temperature increases, H_2 must be highly confined inside the pores of the materials. It has been demonstrated previously that H_2 uptake is the largest in materials with a significant volume of ultramicropores. The confinement of H_2 is amplified in ultramicropores because of overlapping potential from opposing pore walls [12]. In contrast, mesopores do not contribute much to the storage of H_2 [13]. Also, it has been shown that the spherical or cylindrical geometry of the pores hinders the mobility of H_2 to a larger extent than slit-shaped pores [9].

The highest reported H_2 storage density inside a carbon material at 1 bar and 77 K is 18 g dm^{-3} [14]. Currently, the targets set by DOE for the complete H_2 storage systems are to reach the storage density of 40 g dm^{-3} by 2025, the ultimate target to reach being 50 g dm^{-3} at STP [2]. To meet these targets, accurate confirming the effect of pores with specific widths and geometries on H_2 storage capacity and hindrance is essential in developing the optimal carbon material for mobile H_2 storage applications.

1.2 Gas adsorption

Gas adsorption is the adhesion of gas molecules to an interfacial layer, so the concentration of the molecules in the interface exceeds the concentration in the gas phase. The solid material on which the adsorption occurs is called adsorbent, and the gas molecules in the adsorbed state are referred to as adsorbate [15].

Adsorption can be classified into physical adsorption (i.e., physisorption) and chemical adsorption (i.e., chemisorption) based on the type and the energy of the bond formed between the adsorbate and adsorbent. In the case of physisorption, there are van der Waals interactions between adsorbate and adsorbent with the interaction enthalpy of up to 40 kJ mol^{-1}. In the case of chemisorption, on

the other hand, a chemical bond is formed between the adsorbate and the adsorbent with the bond enthalpy of approximately 50−200 kJ mol^{-1} [16]. Physisorption can occur as multilayer adsorption. In contrast, chemisorbed molecules are chemically bound to the surface of the adsorbate, and thus, chemisorption can occur only in the monolayer. Chemisorption is predominantly irreversible, whereas physisorption is always a reversible process. The reverse process of adsorption is called desorption. In thermodynamic equilibrium, the rate of adsorption and desorption processes are equal [15].

During the measurement of a gas adsorption isotherm, the excess adsorption is measured in relation to the equilibrium pressure of the adsorbate at isothermal conditions. At pressures lower than 10 bar, absolute and excess adsorption can be considered equal [17]. The relation of the quantity of adsorbate (gas) to the equilibrium pressure of the adsorbate at isothermal conditions is known as the adsorption isotherm [16]. Usually the pressure of adsorbate, p, is expressed as relative pressure, p/p_0, where p_0 is the saturation pressure of the adsorbate at the measurement temperature.

Table 1. Physical properties of gases used for analysis - temperature (T_m), saturation pressure at T_m (p_0), relative pressure at which the measurement starts (in. p/p_0), self-diffusion coefficient (D_s) and analyzable pore range (w is width of the pore) with the gas.

Gas	T_m / K	p_0 / mbar	in. p/p_0 / unitless	D_s at STP / $cm^2\ s^{-1}$	Pore range / Å
N_2	77	1019	$\sim10^{-7}$	0.172[18]	$7 < w < 500$
Ar	87	1003	$\sim10^{-6}$	0.158[19]	$7 < w < 500$
CO_2	273	34853	$\sim10^{-4}$	0.09[18]	$7 < w < 20$
H_2	77	1013	$\sim10^{-5}$	1.24[19]*	$w < 7$

*Deuterium diffusion into H_2 at T = 288 K, the diffusion of two different isotopes of the same gas is an example of self-diffusion [19].

Due to the distinct physical conditions (Table 1), gas adsorption measurements with different gases provide somewhat different information about the adsorbent. The maximal value of p/p_0 reached in N_2 and Ar isotherms is near one, which means that in the end of the experiment the adsorbates would be liquefied and all the pores would be filled with adsorbate. Thus, N_2 and Ar adsorption isotherms characterize both the micro- and mesopore volumes and surface areas of the material. The adsorption of N_2 and Ar in micropores begins already at low p/p_0 since the measurement of these isotherms is performed at very low temperatures (liquefaction temperatures of N_2 and Ar at

1 bar, respectively). At these conditions, N_2 and Ar diffusion rate into narrow ultramicropores is slow which may result in time-consuming measurements and/or data points which do not correspond to true established adsorption equilibrium. The adsorption equilibrium establishes faster in the case of CO_2 adsorption, since the measurement temperature is higher and adsorption begins at a higher pressure compared to the N_2 or Ar adsorption measurements. Thus, the adsorption isotherms of predominantly microporous materials are more correct to analyze with CO_2 because it is less time-consuming and results in more reliable data. In addition to CO_2, analysis with H_2 is also suitable for characterization of micropores, ultramicropores, and even closed porosity of the adsorbent because H_2 molecule is smaller than other gas molecules and has a higher self-diffusion coefficient, therefore it may have access to pores that are not accessible to other gases [20].

N_2 is a diatomic molecule with a quadrupole moment, meaning that the orientation of the N_2 molecule can depend on the surface chemistry of the adsorbent. Ar, on the other hand, does not exhibit a quadrupole moment and is more inert than the N_2 molecule and thus, may provide more accurate results when there are specific functional groups on the surface of the adsorbent [15]. For example, Lässig et al. [21] reported a difference in the isotherms measured with Ar and N_2 and attributed this difference to the specific interaction of N_2 molecules with the functional groups presented in narrow pore channels of the metal-organic framework. When adsorption isotherms measured with N_2 and Ar are equivalent, then the surface of the adsorbent can be considered chemically inert against the gases used for analysis [20].

1.3 Different types of diffusion

Two kinds of diffusion processes can be distinguished – transport diffusion and self-diffusion. Transport diffusion corresponds to the non-equilibrium state where particles migrate down the concentration (more specifically, the chemical potential) gradient. Transport diffusion coefficient, D_t, is defined by Fick's first law (Equation 1) as the proportionality constant relating a macroscopic flux to a concentration gradient [22].

$$J = -D_t \frac{dC}{dx} \tag{1}$$

where J is diffusion flux, D_t is transport diffusion coefficient, C is concentration, and x is distance.

Self-diffusion takes place under thermodynamic equilibrium, and it describes the translational movement of individual molecules. Self-diffusion coefficient, D_s, quantifies the time dependence of the mean square displacement of a molecule and is defined from ensemble averaging Einstein's equation over a large enough number of particles, N (Equation 2) [22]:

$$D_s = \left(\frac{1}{6N}\right)\sum_{\mathrm{k}=1}^{N}\lim_{t\to\infty}\frac{1}{t}\langle|\boldsymbol{r}_{\mathbf{k}}(t)-\boldsymbol{r}_{\mathbf{k}}(0)|^2\rangle \qquad (2)$$

where D_s is self-diffusion coefficient, $\boldsymbol{r}_{\mathbf{k}}(t)$ is the position of the kth molecule at time t, and angular brackets indicate an ensemble average.

Single-particle diffusion can take place as consecutive short jumps or extend over relatively large distances in the order of nanometers. After several jumps of a particle, the jump mechanism details are lost by averaging. Only a global quantity characterizing the single-particle diffusion process is obtained – the macroscopic self-diffusion coefficient measured over microscopic distances. Random translational diffusion of an atom/molecule corresponds to the Brownian motion – particles are unconstrained and have very weak interactions. Some systems can exhibit phenomena that hinder continuous diffusion, resulting in a jump-like motion with a period of residence time between jumps [23,24]. Some of the models describing this kind of behavior are discussed in Section 1.4.4.

The temperature dependency of a diffusion coefficient (both transport and self-diffusion) is described by an Arrhenius-like equation (Equation 3) [16]:

$$D = D_0 \exp\left(-\frac{E_\mathrm{a}}{RT}\right) \qquad (3)$$

where D is the diffusion coefficient, D_0 is the diffusion coefficient at infinite temperature (maximal diffusion coefficient), E_a is the activation energy of the diffusion process, R is the universal gas constant, and T is the temperature.

In an Arrhenius-type plot, ln(D) is plotted against 1/T and a linear relationship is seen. From the slope, the E_a values can be calculated. E_a is the minimal enery, i.e. energetical barrier that needs to be exceeded for the diffusion process to occur. A high value of E_a implies that the diffusion process depends strongly on temperature, whereas a low value of E_a indicates that the diffusion process is practically independent form temperature [16].

1.4 Neutron scattering

1.4.1 Neutron properties

Neutron is a particle with no electric charge, with a mass of $m = 1.675 \cdot 10^{-27}$ kg and a magnetic dipole moment of $\mu_n = -9.662 \cdot 10^{-27}$ J·T^{-1}. The half-life of a neutron as a free particle is ~10 min. Neutrons interact with atomic nuclei via the strong force or scatter from unpaired electrons via the magnetic dipole-dipole interaction. Neutron radiation penetrates deep into the material, making it possible to study the microscopic properties of bulk samples. Also, neutron radiation is non-destructive, meaning delicate archeological and biological samples can be studied. Neutron scattering cross-sections do not depend directly on the number of electrons per atom (as opposed to X-rays), thus light nuclei (e.g., H, O, C) and isotopes of the same element (e.g., H and D) can be distinguished. In addition, neutrons are used to investigate microscopic magnetic structures and magnetic fluctuations [25].

The wavelength of neutrons used in scattering experiments ranges from 0.5 to 20 Å, which is comparable to atomic sizes and inter-distance spacings. Moreover, the energy window, which ranges from 0.2 to 330 meV, is comparable to normal energy modes in materials. For these two reasons, neutron scattering is suitable for simultaneous investigation of the structural properties of the matter at the atomic to nanometer scale as well as dynamic properties, such as diffusion, lattice vibration, phonons characteristic [25].

1.4.2 The scattering process

A neutron beam incident on a single scattering center and traveling in the direction x can be represented as a plane wave (Figure 1, blue lines). When the neutron scatters from the nucleus, the scattering will be isotropic (with equal probability in any direction) since the range of the nuclear potential is small compared to the wavelength of the incident neutron. As a result, the scattered neutron beam spreads out in spherical wavefronts (Figure 1, red circles). When the scattering center is rigidly fixed, then the interaction is elastic. Thus, there is no exchange of energy and the incident and scattered wave vectors both have magnitude k [26].

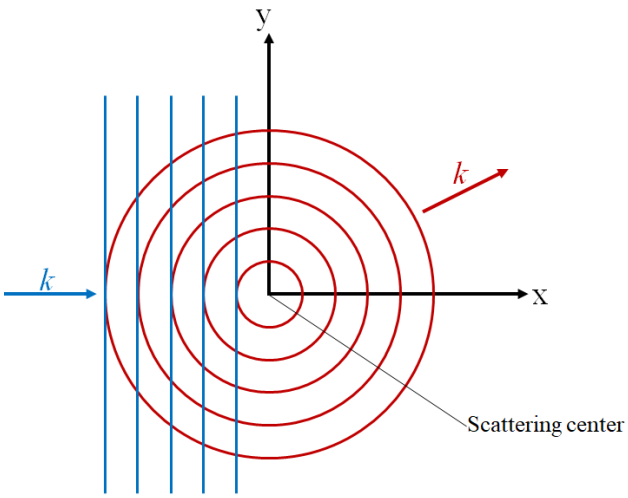

Figure 1. Scattering by a single fixed nucleus. Blue lines denote incident neutron beam as plane waves, red circles denote scattered neutron beam as spherical wavefronts (Recreated according to Ref. [26]).

When the scattering process is not elastic, the energy of the neutron and/or the momentum of the neutron scattering from the atomic nucleus changes. The change in energy (Equation 4) and momentum (Equation 5) are expressed as:

$$E = \hbar\omega = E_{\mathrm{f}} - E_{\mathrm{i}} \tag{4}$$

$$\boldsymbol{Q} = \boldsymbol{k}_{\mathbf{f}} - \boldsymbol{k}_{\mathbf{i}} \tag{5}$$

where E is neutron's energy transfer, $\hbar$ is angular Planck constant, ω is angular frequency, E_{f} and E_{i} are energies of final and incident neutron, respectively, $\boldsymbol{Q}$ is momentum transfer vector, and $\boldsymbol{k}_{\mathbf{f}}$ and $\boldsymbol{k}_{\mathbf{i}}$ are the wave vectors of final and incident neutron, respectively.

The measured quantity is the number of neutrons detected in a solid angle $\delta\Omega$ with energy transfer δE. This quantity is called the double differential scattering cross-section (Equation 6) [24].

$$\frac{\delta^2\sigma}{\delta E \delta\Omega} = \frac{|\boldsymbol{k}_{\mathbf{f}}|}{|\boldsymbol{k}_{\mathbf{i}}|}\left[b_{\mathrm{coh}}^2\, S_{\mathrm{coh}}(\boldsymbol{Q}, E) + b_{\mathrm{inc}}^2\, S_{\mathrm{inc}}(\boldsymbol{Q}, E)\right] \tag{6}$$

where σ is the scattering cross-section, S is the dynamical structure factor and b is the scattering length (coh and inc denote coherent and incoherent contribution, respectively).

Scattering of a neutron from an atom (or a molecule) can be coherent or incoherent. If scattering is coherent, the neutron wave interacts with the whole sample as a unit and the scattered waves from different nuclei interfere with each other. This type of scattering depends on the relative distances between the constituent atoms and, thus, gives information about the structure of

material. In the case of incoherent neutron scattering, a neutron wave interacts independently with each nucleus in the sample, so that the scattered waves from different nuclei do not interfere. This type of scattering may, for example, be due to the interaction of a neutron wave with the same atom but at different positions and different time [26]. Thus, dynamics associated with incoherent scattering are related to uncorrelated self-motion, such as diffusion [27].

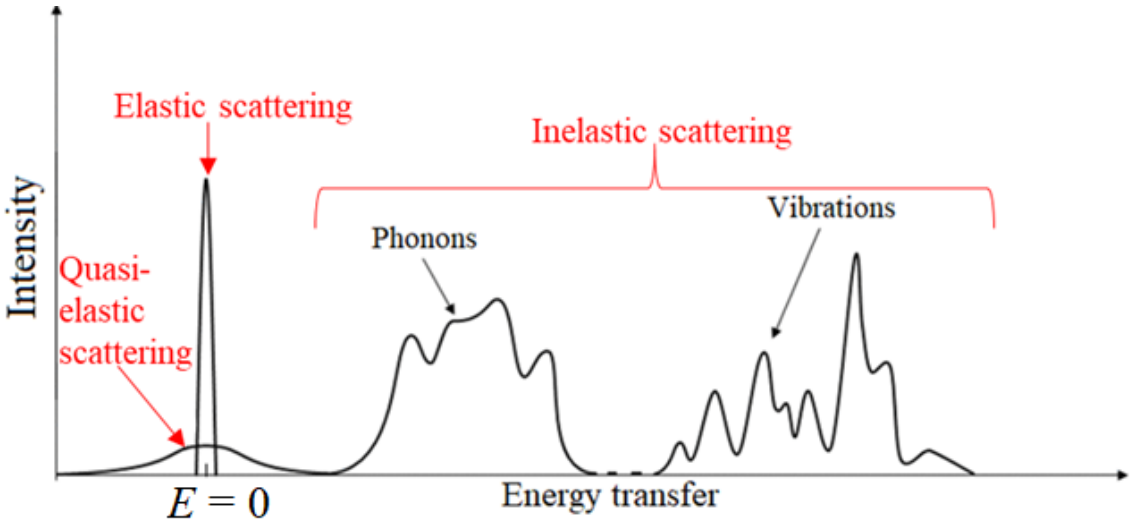

Figure 2. Types of neutron scattering (written in red) by energy transfer (recreated according to Ref[24,25]).

If no atomic or molecular movement occurs with similar energy (and thus, timescale) to the incident neutrons, the scattering process is elastic ($E_f = E_i$). When the atom (or molecule) from which neutron scatters is moving within the timescale being similar to the experimental time window, then energy may be transferred from or to the incident neutron. Thus, scattering is no longer elastic ($E_f \neq E_i$). When the change in neutron energy is small ($E \leq 2$ meV), and the peak maximum is situated at $E = 0$, the scattering process is called quasi-elastic. When $E > 2$ meV, the scattering process is named inelastic. Inelastic scattering is associated with phenomena occurring with well-defined energies like phonons and vibrations (Figure 2) [27].

1.4.3 Quasi-elastic incoherent neutron scattering from H_2

H_2 has a large incoherent scattering cross-section ($\sigma_{inc} = 80.26$ barn) and a small coherent scattering cross-section ($\sigma_{coh} = 1.76$ barn) [28]. Thus, when the neutron scatterer is H_2, coherent contribution

can be considered negligible and only the incoherent contribution has to be taken into account [24]. Equation 6 can be reduced to Equation 7:

$$\frac{\delta^2\sigma}{\delta\Omega\delta E} = \frac{|\boldsymbol{k_f}|}{|\boldsymbol{k_i}|} b_{inc}^2 S_{inc}(\boldsymbol{Q}, E) \quad (7)$$

In reality, $S_{inc}(\boldsymbol{Q},E)$ cannot be measured directly. This is replaced with the experimental dynamic structure factor $S_{exp}(\boldsymbol{Q},E)$, which is proportional to the convolution of the incoherent dynamic structure factor of H_2 $S_{H2}(\boldsymbol{Q},E)$ with the resolution function $R(\boldsymbol{Q},E)$ of the spectrometer given with Equation 8:

$$S_{exp}(\boldsymbol{Q}, E) = S_{H2}(\boldsymbol{Q}, E) * R(\boldsymbol{Q}, E) \quad (8)$$

where symbol * denotes the convolution product.

$S_{H2}(\boldsymbol{Q},E)$ can be composed of multiple components, such as elastic and quasi-elastic components. Elastic component denotes scattering from particles which motion is too slow to be observable within the experimental resolution. Quasi-elastic component (i.e. quasi-elastic broadening) rises from motions which take place within instrument experimental time window and are not resolution limited. When resolved motions take place in multiple time scales, the quasi-elastic component can consist of multiple components of quasi-elastic scattering. Motions of particles which are faster than the experimental time window contribute to the flat background [27].

With a QENS instrument, the time scale studied is set by the width of the instrument energy resolution, typically at least 0.1 meV. Higher resolution enables to study slower motions. The length scale studied with QENS is set by the wavelength of incident neutrons, λ, since the maximal Q is set by $Q = 4\,\pi\,\lambda^{-1}$.

1.4.4 Translational jump diffusion models

The Q-dependence of the quasi-elastic broadening in the case of continuous diffusion is governed by the Fick's law (Equation 9, Figure 3) [29].

$$\Gamma(Q) = D\,Q^2 \quad (9)$$

where Γ is HWHM of the quasi-elastic broadening, Q is the magnitude of the $\boldsymbol{Q}$-vector and D is the diffusion coefficient.

The diffusion process is not continuous, when systematic deviations from Fick's law are observed at large Q values (i.e short length scale in real space). The models that consider the deviations from continuous diffusion process are called translational jump diffusion models. The derived parameters resulting from fitting the calculated data with translational jump diffusion models are diffusion coefficient D, residence time τ (i.e., the time a particle spends at a position before it jumps to a new position) and mean jump length l [23,24]. Different jump diffusion models have been proposed by Chudley and Elliott [30], Hall and Ross [31] and Singwi and Sjölander [32] (Figure 3). At small Q-values the Γ vs Q relation of all jump diffusion models are similar to Fick's law (Equation 9), but they differ in the assumed jump length distributions, which result in deviations at large Q-values [29].

The model proposed by Chudley and Elliott assumes that all residency sites are energetically equivalent and only jumps to the nearest sites are allowed, meaning that the jump lengths are constant (Equation 10) [30]. This model was developed considering a liquid in quasi-crystalline form and has been applied in studying atoms diffusion through a lattice [27].

$$\Gamma(Q) = \frac{\hbar}{\tau}\left(1 - \frac{\sin(Ql)}{Ql}\right) \tag{10}$$

where l is the mean jump length and τ is the residence time.

The model proposed by Hall and Ross assumes that the jump lengths follow a Gaussian distribution (Equation 11). Hall-Ross model describes jump diffusion in a restricted volume, for example in narrow pores [31].

$$\Gamma(Q) = \frac{\hbar}{\tau}\left(1 - \exp\left(-\frac{Q^2\tau D}{3}\right)\right) \tag{11}$$

The model proposed by Singwi and Sjölander suggests an exponential distribution of jump lengths (Equation 12). This model characterizes diffusion which alternates between oscillatory and directed motions [32]. It was developed for liquid water and it was assumed that each molecule oscillates for a time τ before undergoing continuous linear diffusive motion [27].

$$\Gamma(Q) = \frac{\hbar D Q^2}{1 + DQ^2\tau} \tag{12}$$

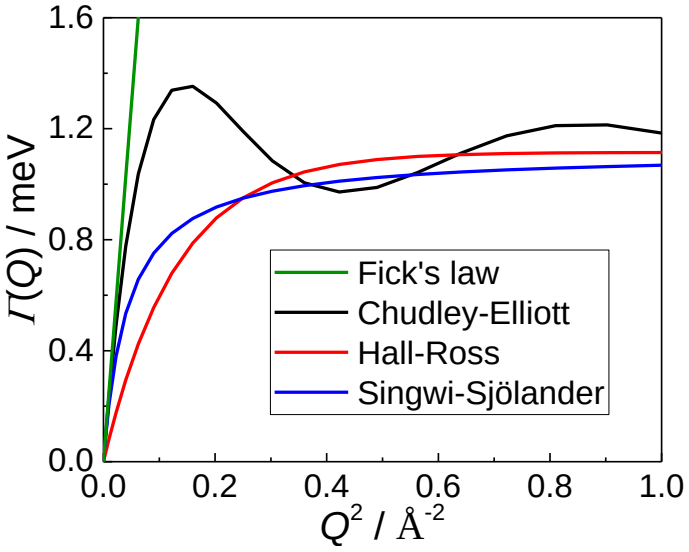

Figure 3. Continuous diffusion (Fick's law), Chudley-Elliott, Hall-Ross and Singwi-Sjölander jump diffusion models.

1.5 Previous studies of H_2 diffusion in porous carbons with QENS

The exact experimental conditions, i.e. the temperature and applied H_2 loading pressure range need to be considered while comparing the diffusion coefficients of H_2 in different adsorbents reported in previous studies. Contescu et al. [12] studied H_2 diffusion in two carbon materials with high surface areas, PFAC and UMC, at low temperatures from 25 K to 37 K. Bahn et al. [33,34] studied the H_2 diffusion in a carbon aerogel, CA, and so-called highly porous carbon, HPC, in a temperature range from 10 K or 5 K to 80 K. In addition to the used carbon adsorbent and temperature range, the amount of H_2 adsorbed in the samples impacts the average self-diffusive nature of H_2. The amount of H_2 adsorbed in the studies of Bahn et al. was relatively high. Namely half of the surface of the studied carbons CA and HPC was covered in a monolayer of H_2 molecules. In contrast, in the study of Contescu et al. the H_2 loading pressure was selected to ensure a relatively low surface coverage of PFAC and UMC. When the surface coverage and the temperature is low, only the adsorption sites which confine H_2 the strongest are occupied and, thus, the resulting activation energy, E_a, will also be higher irrespective of the different porous structure of studied carbons (Table 2).

In some studies, the H_2 motion has been seen to occur in multiple distinguishable time scales [34]. Bahn et al. [34] concluded that H_2 exhibited rotational and translational diffusion dynamics in HPC, whereas the mobility of H_2 adsorbed in PFAC, UMC, and CA was characteristic for motion in one

timescale [12,33]. Moreover, the diffusion of H_2 has been seen to occur via different mechanisms. This means that different jump diffusion models have been applied – Chudley-Elliott model for PFAC, UMC and CA; Singwi-Sjölander model for HPC and C900 [9,12,33,34]. The various experimental conditions and analysis methods make it complicated to use the published diffusion parameters to compare the porous carbons based on how well they confine H_2.

Table 2. PFAC, UMC, CA and HPC pore structure characteristics and activation energies.

Sample	S_{BET} / $m^2\ g^{-1}$	V_{tot} / $cm^3\ g^{-1}$	V_{micro} / $cm^3\ g^{-1}$	E_a / kJ mol^{-1}	Surface coverage	Ref
PFAC	1530	0.99	0.26	1.82	low	[12]
UMC	2540	1.42	0.71	1.49	low	[12]
CA	808	0.95	0.33	0.72	high	[33]
HPC	1712	2.75	--	1.06	high	[34]
Mo_2C 900	1370	1.43	0.30	1.04	low	[9]

S_{BET} – surface area calculated from BET method applied to N_2 adsorption data; V_{tot} – total pore volume calculated at p/p_0 = 0.95 from N_2 adsorption data; V_{micro} – micropore volume; E_a – activation energy.

CA has relatively low S_{BET}, V_{tot} and V_{micro} which indicates a relatively low ratio of micropores. The amount of adsorbed H_2 was relatively high, meaning that H_2 was probably adsorbed not only in the micro-, but also in the mesopores. H_2 mobility is not hindered in mesopores, giving rise to a low E_a. HPC has the highest V_{tot}, but an insignificant fraction of micropores which could not be reliably calculated. V_{micro} of HPC is insignificant and the surface coverage with H_2 molecules is relatively high, meaning H_2 is adsorbed not only in the micropores, but also in the mesopores. In these mesopores the mobility of H_2 is less restricted which is reflected in a relatively low E_a value, similarly with CA. Mo_2C 900, investigated previously in Ref. [9], has a relatively small fraction of micropores. The E_a value is also relatively low, indicating that H_2 weakly confined in samples with low micropore volumes.

UMC is a relatively microporous material characterized by a relatively high S_{BET} value and approximately half of the total porosity (V_{tot}) is from micropores (V_{micro}). PFAC, on the other hand, has an average S_{BET} and approximately quarter of V_{tot} is from V_{micro}, but E_a values of both materials are the highest out of the five materials indicating the strongest confinement of H_2. The high E_a

values can be attributed not only to the high ratio of micropores, but also to the low temperature range as H_2 mobility is more restricted when temperatures are near liquid H_2 temperature (20 K) in comparison to higher temperatures, where H_2 is in gas phase. The amount of adsorbed H_2 was relatively low, so H_2 was adsorbed mostly in the micropores which restrict the mobility of H_2 more than mesopores, giving rise to higher E_a-s than for CA and HPC, where H_2 was adsorbed also in the mesopores, in addition to micropores.

The influence of the pore geometry on the confinement of H_2 has also been previously investigated. It was demonstrated that the cylindrical geometry of the pores confines H_2 to a larger extent than the slit-shape geometry of the pores [9].

2. Experimental

2.1 Synthesis of Mo_2C derived carbons

Molybdenum carbide (Mo_2C) was placed onto a stationary quartz bed and synthesized by chlorination reaction method at reaction temperatures 700 °C, 800 °C and 900 °C for approximately 4.5 h. The chemical reaction equation is as follows (Equation 13) [7]:

$$Mo_2C + 5Cl_2 \rightarrow C + 2MoCl_2 \quad (13)$$

To remove contaminants (e.g., residual chlorine, chlorides, and oxygen-containing functional groups) from the surface of the material, the carbon powder was treated with H_2/He mixture at 800 °C for 1.5 h [7]. The samples are noted according to their chlorination temperatures in degrees of Celsius as C700, C800 and C900, respectively.

2.2 Gas adsorption

C700, C800 and C900 were outgassed at temperature and pressure of 300 °C and 13 μbar, respectively, for 12 h before the gas adsorption measurements were conducted. Gas adsorption measurements were conducted on ASAP 2020 (Micromeritics, USA) with four different gases at three different temperatures. N_2 and H_2 isotherms were measured at −196 °C (77 K), Ar isotherms at −186 °C (87 K) and CO_2 isotherms at 0 °C (273 K), respectively.

2.2.1 Specific surface area, pore volume and pore size distribution

The specific surface area, S_{BET}, of the samples was calculated from N_2 adsorption isotherms according to the BET theory. The BET theory describes multilayer adsorption and presumes that all adsorption sites are energetically equivalent, the system is microscopically flat and there are no specific interactions between adsorbate molecules [35]. The total pore volume (V_{tot}) was calculated based on the amount of adsorbed N_2 near the saturation pressure, $p/p_0 = 0.95$.

To calculate the pore size distribution, adsorption isotherms of H_2, CO_2, N_2 and Ar were measured and simultaneously analyzed with SAIEUS (Micromeritics, USA) software [36]. SAIEUS applies two-dimensional non-local density functional theory for heterogeneous surface (2D-NLDFT-HS) to calculate the pore size distribution, cumulative pore area (S_{DFT}), and the cumulative pore volume (V_{DFT}). 2D-NLDFT-HS assumes an energetically heterogeneous surface of the adsorbent and a certain pore shape [37,38]. The pore size distributions, S_{DFT}, and V_{DFT} were calculated by fitting the experimental adsorption isotherms with 2D-NLDFT-HS models (see fitting results in Appendix D) (J. Jagiello has developed the new version (personal communication), September 29, 2020). Including the H_2 adsorption isotherm data in the pore size calculation extends the lower limit of the pore size below that of standard N_2 measurement. These smaller pores are not characterized by N_2 isotherms but they play a significant role in the uptake and confinement of H_2 [36].

2.2.2 Analysis of the porous structure

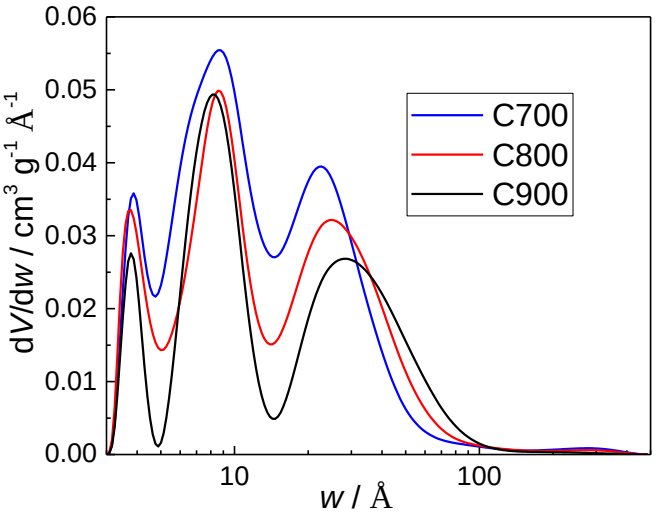

Figure 4. C700, C800 and C900 (noted on the graph) pore size distributions calculated with a combination of N_2, Ar, CO_2 and H_2 2D-NLDFT-HS models.

When the pore width is small, i.e., the distance between the pore walls is short, then it contributes mostly to the surface area and less to the pore volume. All samples have a similar pore size distribution and the materials under study exhibit ultramicro-, micro- and mesopores (Figure 4). The materials differ somewhat in the ratio of pores with a certain size. Generally, with the increase of the CDC chlorination temperature, the specific surface area and volume of pores of the CDC decreases. C700 has the highest volume of micro- and ultramicropores and the lowest volume of mesopores. C800 has an average and C900 has the lowest micro- and ultramicropore volume of the samples, but their mesopore volume is higher than that of C700-s (Table 3).

Table 3. Specific surface areas, S_{BET} (calculated according to BET theory) and S_{DFT} (calculated from 2D-NLDFT-HS model), and pore volumes, V_{tot} (calculated near N_2 saturation pressure, $p/p_0 = 0.95$) and V_{DFT} (calculated from 2D-NLDFT-HS model).

	S_{BET} $m^2\ g^{-1}$	S_{DFT} $m^2\ g^{-1}$	V_{tot} $cm^3\ g^{-1}$	V_{DFT} $cm^3\ g^{-1}$	V_{ump} $w < 7$ Å $cm^3\ g^{-1}$	V_{micro} $7 < w < 20$ Å $cm^3\ g^{-1}$	V_{meso} $20 > w > 500$ Å $cm^3\ g^{-1}$
C700	2150	1810	1.76	1.61	0.12	0.49	1.00
C800	1760	1500	1.65	1.52	0.08	0.35	1.09
C900	1370	1290	1.43	1.42	0.07	0.26	1.09

The numeric values of surface areas (S_{BET} and S_{DFT}) and pore volumes (V_{tot} and V_{DFT}) were calculated applying different models and methods, so they are not numerically exactly comparable (Table 2) but follow the same trend as the pore size distributions (Figure 3). $S_{DFT} < S_{BET}$ because S_{DFT} is calculated applying 2D-NLDFT-HS, which considers pores smaller than 300 Å. In contrast, BET theory considers all the pores accessible to the adsorbate (in this case, N_2) at the measurement conditions (Table 1).

2.3 Quasi-elastic neutron scattering

2.3.1 Experimental details

H_2 diffusion in C700, C800 and C900 was investigated with quasi-elastic neutron scattering (QENS) method. QENS measurements of C900 were conducted in March 2017 and C700 and C800 in December 2018 at Helmholtz Zentrum Berlin on time-of-flight spectrometer NEAT'2016 [39] (energy resolution of 100 μeV) using BER II as a neutron source.

All three samples were outgassed to remove any contaminants from air and other possible adsorbed species. C900 was outgassed for 17 h at 300 °C, C700 and C800 were outgassed for 52 h at 250 °C. After the outgassing, the samples were transferred into an aluminum sample holder. Before the QENS measurement, the signal from the vanadium cell and the empty sample holder was measured to calibrate the detectors and subtract the background.

The measurement plan for all three samples was identical. At first, the signal was measured from carbon samples under vacuum at 50 K, 60 K, 70 K, 80 K, 90 K and 100 K. After that, the samples were loaded with H_2 at 68 mbar in case of C700 and 86 mbar in case of C800 and C900 (low loading pressure) at 77 K and the adsorption equilibrium was let to establish during approximately 1 h. In the sample cell, there was 4 mmol of H_2 for C700 and C800 and 3 mmol of H_2 for C900 per 1 g of the sample (Appendix A, Table A2). Thereafter, the temperature was decreased to 20 K, then increased to 50 K and measurements up to 100 K were conducted with neutrons with the wavelength of 5 Å (C700 was also measured at 30 K and 40 K). Measurements at the loading pressure of 1 bar at 77 K (moderate loading pressure) and 10 bar at 77 K (high loading pressure) were performed identically. Once the equilibration was established at 77 K, the H_2 amounts in the sample holder per 1 g of CDC sample at different H_2 loading pressures used are brought in Appendix A Table 2A.

2.3.2 Data Analysis

Data reduction, including normalization with vanadium, corrections for detector efficiency and background subtraction was performed with Mantid software package [40]. Scattering data binning was performed in three different Q ranges (from 0.2 to 2.45 $Å^{-1}$, from 0.25 to 2.5 $Å^{-1}$ and from 0.3 to 2.4 $Å^{-1}$ with a step of 0.15 $Å^{-1}$) and in two different E ranges (at low loading pressure from −2 to 2 meV and at moderate and high loading pressure from −3 to 2 meV with the step of 8 μeV).

Analysis and visualization of the data were performed in using software OriginPro 2016. As the first step of the analysis, the signal measured from the sample under vacuum was subtracted from the incoherent dynamic structure factors of sample loaded with H_2 to analyze only the contribution of adsorbed H_2.

The dynamic structure factor of H_2, $S_{H2}(\boldsymbol{Q},E)$ (Equation 8), was fitted with the model incoherent dynamic structure factor, $S_{model}(\boldsymbol{Q},E)$ (Equation 14).

$$S_{model}(\boldsymbol{Q},E) = A_0(\boldsymbol{Q})\,\delta(E) + \sum_{i=1}^{n} A_i(\boldsymbol{Q}) L_i(E,\Gamma_i) \quad (14)$$

where $\delta(E)$ is the Dirac delta function, $L(E,\Gamma)$ is the quasi-elastic component with the half width at half maximum (HWHM) Γ, parameter A_0 is the fraction of the elastic scattering signal associated with the solid-like immobile H_2, A_1 is the fraction of the quasi-elastic signal associated with partially mobile H_2 and n denotes the number of quasi-elastic components.

Dirac delta function $\delta(E)$ describes the elastic scattering and has a finite intensity at E=0. In practice, the elastic line is broadened by the resolution function of the instrument (Equation 8). For NEAT, the resolution, $R(\boldsymbol{Q},E)$, can be described with the Gaussian distribution (Equation 15)[23]. Therefore, for the present work, the Gaussian represents the elastic component which denotes H_2 with mobility too slow to be observed with the NEAT instrument using 0.1 meV resolution.

$$G(E) = \frac{1}{w\sqrt{\frac{\pi}{4\ln(2)}}}\, e^{\frac{-4\ln(2)E^2}{w^2}} \quad (15)$$

where G is the Gaussian distribution function, E is the neutron's energy change. The FWHM of the Gaussian, w, is often referred to as the resolution of the instrument[41].

The quasi-elastic broadening, which occurs due to molecular motion, e.g., self-diffusion, is described by a Lorentzian distribution (Equation 16) [23].

$$L(E) = \frac{2}{\pi}\,\frac{2\Gamma}{4E^2 + (2\Gamma)^2} \quad (16)$$

where L is the Lorentzian distribution function, E is the neutron's energy change and Γ is the HWHM of the Lorentzian distribution function.

The H_2 structure factors were fitted with a combination of a Gaussian distribution function and one Lorentzian distribution function (Equation 17) or two Lorentzian distribution functions (Equation 18), depending on the H_2 loading pressure and on the temperature applied (Figure 5a and 5b).

$$S_{model1}(\boldsymbol{Q},E) = A_0(\boldsymbol{Q})\,\delta(E) + A_1(\boldsymbol{Q})\,L(E,\Gamma_1) \quad (17)$$

$$S_{model2}(\boldsymbol{Q},E) = A_0(\boldsymbol{Q})\,\delta(E) + A_1(\boldsymbol{Q})\,L_1(E,\Gamma_1) + A_2(\boldsymbol{Q})\,L_2(E,\Gamma_2) \quad (18)$$

When fitting with multiple Lorentzian distribution functions, H_2 mobility in the multiple different time scales is presumed – narrow Lorentzian (i.e., quasi-elastic component 1, QE1) describes the slower H_2 motion (Figue 5a) and broader Lorentzian (i.e., quasi-elastic component 2, QE2) describes the faster H_2 motion (Figure 5b).

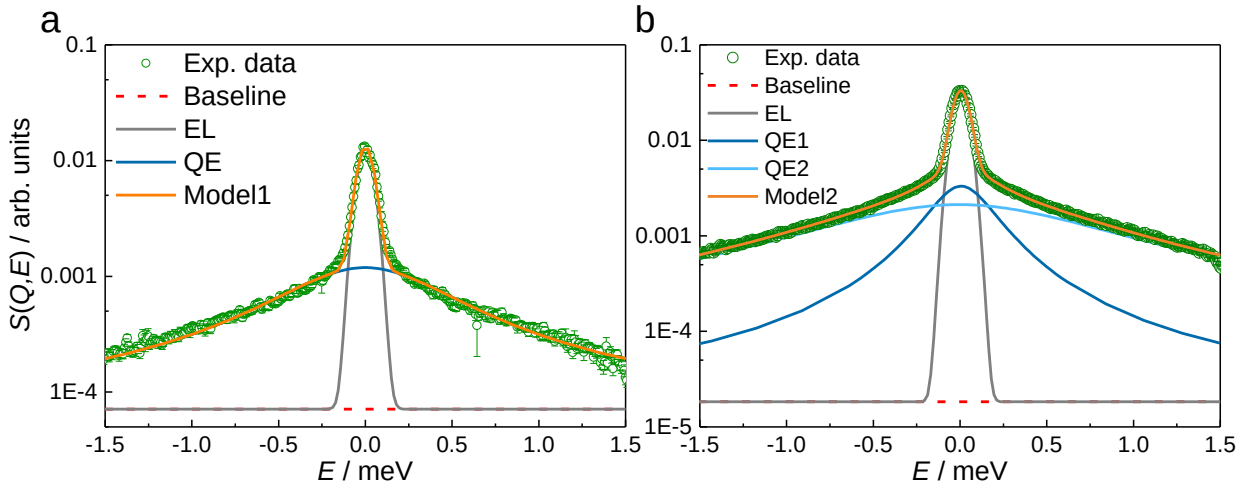

Figure 5. Example of fitting experimental dynamic structure factor $S(Q,E)$ of H_2 adsorbed in C700 at Q = 0.875 Å^{-1} at 70 K with a) Equation 17 at low loading pressure and b) Equation 18 at moderate loading pressure.

2.4 Results and discussion

2.4.1 H_2 adsorption in ultramicro-, micro- and mesopores

When H_2 loading pressure is low, approximately 7% of all available pore volume of the samples are filled with H_2 at 50 K. Assuming that smaller pores are filled first, the amount of H_2 introduced to the sample cell at low loading pressure is adsorbed predominantly in ultramicropores (Figure 6a and Appendix A) [42,43]. Since the pressure reading in the sample cell at temperatures ≤ 50 K indicated a low vacuum ($p \leq 0.0023$ bar, Appendix A, Table A3), it can be concluded that H_2 was strongly confined in the ultramicropores of the samples at $T \leq 50$ K.

Approximately 30% of all available pore volume of the sample is filled with H_2 at moderate H_2 loading pressure at 50 K. An estimation of the pore occupancy indicates that H_2 is adsorbed not only in ultramicropores but also in micropores (Figure 6b and Appendix A). As with the adsorbed H_2 amount at low loading pressure, the pressure reading in the sample cell at $T \leq 50$ K indicates the presence of reduced pressure ($p \leq 0.4$ bar).

At high loading pressure of H_2, all available volume of the samples' pores are filled with H_2 (Figure 6c), i.e., H_2 was adsorbed in ultramicro-, micro- and mesopores.

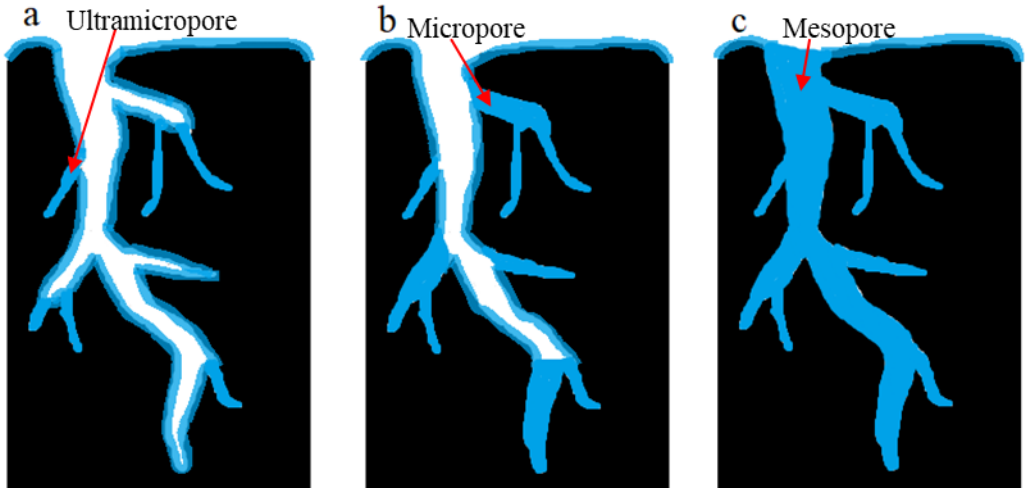

Figure 6. Pore occupancy at 50 K at a) low, b) moderate and c) high H_2 loading pressure.

The change in the fractions of the elastic (onward denoted as EL and A_0) and quasi-elastic scattering components in the structure factor (onward denoted as QE and A_i) in Equation 17 and 18 induced by temperature and pressure is seen in Figure 7. Moreover, in the cases where the QE signal consisted of two components, the fractions of these two components are shown in Figure 7.

At low H_2 loading pressure, most of the H_2 is adsorbed in the ultramicropores (Figure 6a) and a large amount of H_2 adsorbed is immobile at 50 K and 60 K. This is indicated by the large percentage of the elastic component demonstrated in Figure 7a. As the temperature increases, the fraction of the QE component also increases, indicating the increase in the amount of mobile H_2.

The mobility of H_2 adsorbed in the ultramicropores of C700 was also investigated at temperatures of 30 K and 40 K. However, as the quasi-elastic broadening could not be accurately detected, it was concluded that a large amount of H_2 was immobile.

At moderate H_2 loading pressure, H_2 is adsorbed in micropores in addition to ultramicropores (Figure 6b). The fraction of the QE component is larger in the whole temperature range in comparison to filled ultramicropores (Figure 7b) due to larger amount of H_2 in the pores. At 70 K, it is evident that H_2 is diffusing in two timescales and thus, two Lorentzian functions (Equation 18) are needed for the deconvolution of the data (Figure 5b). Mobility of H_2 in different time scales

can be attributed to the restricted motion of the liquid-like H_2 adsorbed on the surface of the pores and H_2 forming subsequent layers in micro- and mesopores.

Application of the two-Lorentzian fitting functions (Equation 18) for data measured at $T \geq 70$ K resulted in better reduced chi-squared fitting statistics, presented in Appendix B. However, at T of 50 K and 60 K, the slower QE component could not be reliably deconvoluted as the amount of the slower moving H_2 was too low or the mobility was too slow to be measured with the NEAT spectrometer under specific conditions used in this experiment (Section 2.3), thus staying below the resolution function.

The fraction of immobile H_2 was lowest in case of highest H_2 loading amounts (Figure 7c), in which case all the pores were filled with H_2 (Figure 6c). Thus, the mobility of H_2 was even less restricted as the fraction of the QE component was large. Like the moderate H_2 amount, H_2 diffusion has been observed in two different time scales, which again agrees well with the fitting statistics (Appendix B).

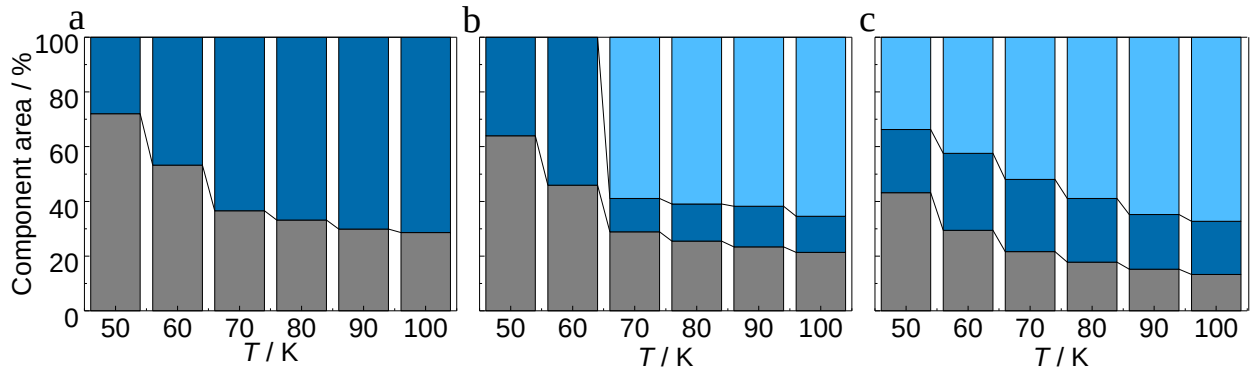

Figure 7. Narrow and broad QE components (dark, A_1, and light blue, A_2, respectively) and EL component (gray, A_0) fractions in the total signal of the C800-s H_2 spectra at $Q = 0.775$ Å^{-1} when a) ultramicropores are filled, b) micro- and ultramicropores are filled and c) all the available pores are filled. The sum of the components is unity, i.e. $A_0 + \sum_{i=1}^{n} A_i = 1$, where n denotes the number of QE components and A_0 and A_i denote EL and QE scattering fractions, respectively. See Appendix C for QE and EL component fractions of C700, C800 and C900 at different Q-values.

2.4.2 Residence times and jump lengths

To calculate the parameters describing H_2 mobility, i.e. the residence times, the jump lengths and the diffusion coefficients, the relations of Γ vs Q were fitted with the jump diffusion models (See 1.4.4) in the Q-range of 0.475−1.175 Å^{-1}. When H_2 was adsorbed only in ultramicropores, the Γ vs Q were fitted with Hall-Ross jump diffusion model as it characterizes diffusion within a

restricted volume (Figure 8). When H_2 was adsorbed also in micropores (moderate loading pressure) and all available pores (high loading pressure), the mobility of H_2 was less hindered by the pore size. Thus, all other Γ vs Q relations corresponding to moderate and high loading pressures, were fitted with Singwi-Sjölander jump diffusion model as the diffusion is assumed to alternate between oscillatory and direct motion (Appendix H).

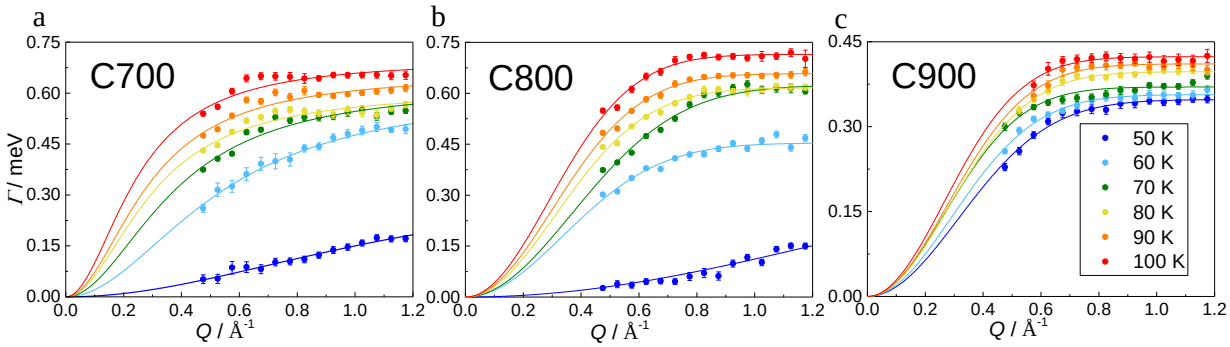

Figure 8. Variation of HWHM of the QE component, Γ, over momentum transfer vector Q at T values from 50 K to 100 K and the corresponding Hall-Ross jump model fitting results to the experimental data (seen as lines) at low H_2 loading pressure for a) C700, b) C800 and c) C900, respectively.

The residence times obtained from the fitting data are presented in Appendix G. As the T increased, the residence times of H_2 adsorbed in ultramicropores reduced from 3 ps to 1 ps, from 2 ps to 0.2 ps when H_2 was adsorbed in micro- and ultramicropores and from 1 ps to 0.03 ps when H_2 was adsorbed in all available pores. With the increase of the amount of adsorbed H_2, the residence times of both slower- and faster-moving components exhibit a decrease for all samples, showing that when H_2 is adsorbed in wider pores, the mobility of H_2 is less hindered.

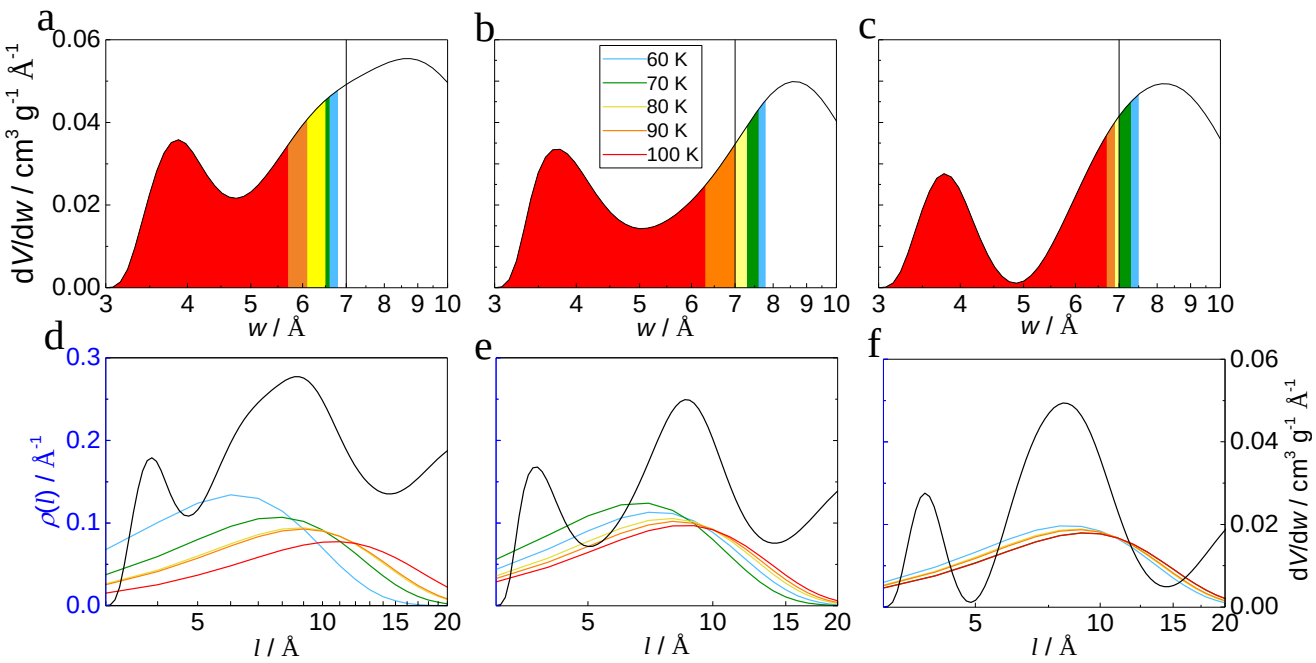

Figure 9. Pore size distribution (black lines) and the ratio of filled ultramicropores of a) C700, b) C800 and c) C900 at adsorbed H_2 amount of 3−4 mmol g^{-1} (vertical black lines denote the upper value of the width of ultramicropores). Pore size distributions (black lines) and jump length distributions of H_2 adsorbed in the ultramicropores of d) C700, e) C800 and f) C900 at *T* values ranging from 60 K to 100 K.

The level of pore occupancy was estimated assuming that the smallest pores are filled first and the density of adsorbed H_2 is similar to the density of liquid H_2 (Figure 9a-c). At the lowest H_2 amount in the sample cell, the ultramicropores of C700 are not completely filled (Figure 9a), whereas the ultramicropores of C800 and C900 are filled at $T \leq 90$ K and H_2 is also adsorbed in some of the micropores (Figure 9b-c).

The jump length distributions were plotted alongside the pore size distribution in Figure 9d-f and it is evident that with the increase in *T*, the H_2 jump length distributions become wider and, thus, the H_2 molecules can and will perform longer jumps. In case of C700, where H_2 jumps occur only in the ultramicropores, the increase in jump lengths is most evident, i.e. from 4.4 Å to 7.6 Å (Appendix F). Since the density of H_2 molecules decreases inside the ultramicropores with the increase in *T*, there is more room for the mobile H_2 to perform longer jumps and the mobile H_2 has more energy to perform longer jumps. At $T \leq 70$ K, the jump lengths of H_2 adsorbed in C700 are shorter than for C800 and C900, as H_2 adsorbed in C800 and C900 at 60 K and 70 K performs some of the jumps in micropores, whereas H_2 adsorbed in C700 performs jumps prevalently in

ultramicropores. The increase in T does not have that notable effect on the jump lengths of H_2 adsorbed in the ultramicropores of C800 and C900 (Figure 9e-f) as the jump length distributions are similar at $T \geq 80$ K.

2.4.3 Diffusion coefficients of H_2 at different pore occupancies

The established self-diffusion coefficients (D) for H_2 are shown in appendix E and are presented graphically in Figure 10. The D values of gaseous H_2 at STP brought in Ref. [19] are higher in orders of magnitude than the D values of H_2 adsorbed in the pores. As the T increases, the D values of adsorbed H_2 increase (Figure 10) since the increase in T induces faster motion and desorption of H_2 molecules.

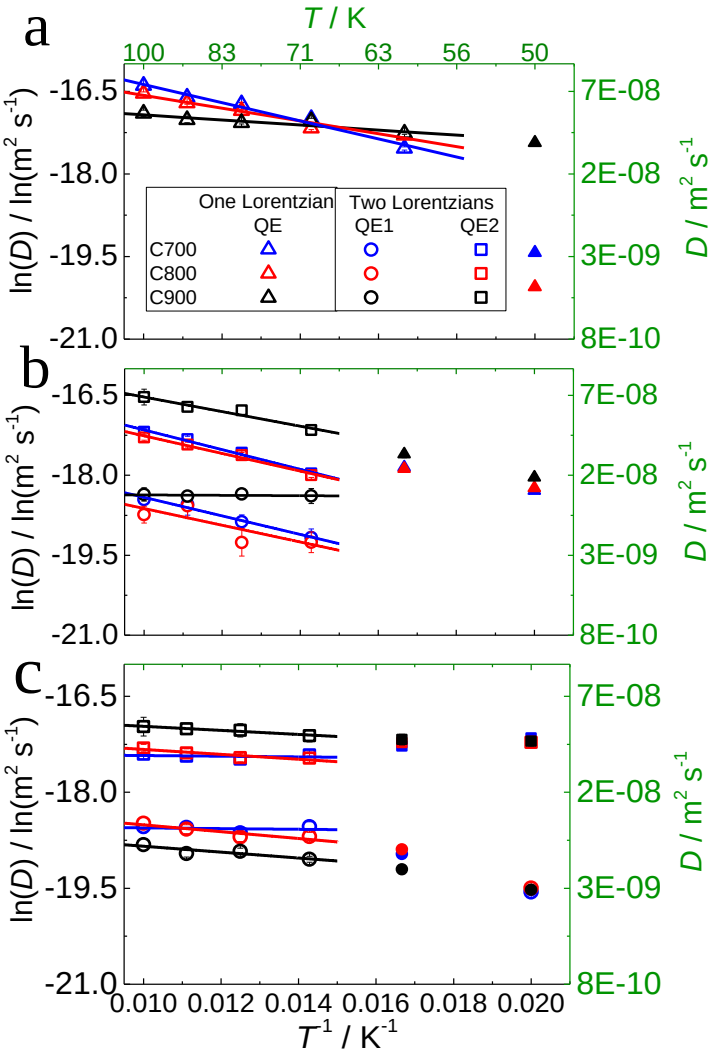

Figure 10. Arrhenius type plots of *D* values obtained in the *T* range from 50 K to 100 K when H_2 was adsorbed in a) ultramicropores, b) micro- and ultramicropores and c) all the available pores. The fit of the linearized Arrhenius equation is given by lines, filled data points have been excluded from the linear fit.

The *D* values of adsorbed H_2 at lower *T* range (50 K) are somewhat different compared to the higher *T* series (≥60 K). Namely, when H_2 was adsorbed only in the ultramicropores of C700 and C800, the *D* values are remarkably lower at 50 K compared to the *D* values at a higher *T* range (Figure 10a). The difference of *D* values at lower *T* range is attributed to the very strong confinement of H_2, which has been established for C700 and C800 but not for C900 and this effect has been more thoroughly investigated in Ref. [10].

At *T* from 80 K to 100 K, the *D* values for H_2 adsorbed in ultramicropores are similar for C700 and C800 and higher than that for C900 (Figure 10a, Appendix E). The *D* values of H_2 adsorbed in ultramicropores (Figure 10a) are larger compared to the *D* values of H_2 adsorbed micro- and ultramicropores (Figure 10b). This can be explained by the immobile H_2 adsorbed in ultramicropores. Namely, when H_2 was adsorbed only in ultramicropores, considerable amount of the H_2 was immobile. Consequently, the amount of mobile H_2 is smaller and has more free volume to diffuse, which results in higher *D* values.

The diffusion of H_2 in C700 and C800 occurs at quite similar rate at a certain *T* within the *T* range from 70 K to 100 K when H_2 is adsorbed in micro- and ultramicropores (Figure 10b). This is true for both QE1 and QE2. However, the corresponding *D* values for H_2 in C900 are larger than for C700 and C800, showing that H_2 is more mobile and not so restricted in comparison to C700 and C800 at the *T* range from 70 K to 100 K. This shows the effect of the different pore size distribution on the diffusion rate of H_2. Namely, when H_2 is adsorbed in a sample with larger micro- and ultramicropore volume, it is more confined.

It is evident from Figure 10b that H_2 adsorbed in micro- and ultramicropores of C700 and C800 at 50 K and 60 K do not follow the same linear trend as the *D* values at 70−100 K. This is mainly because of the very strong confinement of H_2 mentioned previously (and in Ref. [10]). Moreover, the dynamic structure factors of H_2 in the higher *T* range were fitted with the two-Lorentzian model (Equation 18), indicating motion in two timescales. In contrast, the dynamic structure factors at 50 K and 60 K were fitted with the one-Lorentzian model (Equation 17), indicating motion in one timescale.

The *D* values obtained from QE1 and QE2 of H_2 adsorbed in all the available pores of C700 and C800 (Figure 10c) are generally higher than the corresponding *D* values for H_2 in micro- and ultramicropores (Figure 10b). This difference is attributed to the higher amount of adsorbed H_2 in the former case. However, a different trend is seen for C900. The *D* values (Figure 10c) show that C900 restricts the H_2 mobility in the QE1 timescale more than in C700 and C800, whereas the mobility of adsorbed H_2 in the QE2 timescale is higher for C900 than for C700 and C800.

2.4.4 Activation energies of H_2 at different pore occupancies

The *D* values presented in Figure 10 exhibit an Arrhenius-like behavior and thus, the activation energy of the diffusion process (E_a) was calculated from the slopes of the graphs (Table 3) and the maximal diffusion coefficients (D_0) were calculated from the intercepts (Appendix I). The *D* values at low *T* values (filled symbols) were excluded from the analysis for C700 and C800 because of the strong H_2 confinement. Additionally, the *D* values for C900 at the same *T* values were excluded to obtain comparable results with C700 and C800. The calculated E_a-s are presented in Table 4.

Table 4. Activation energies of the diffusion process (E_a) in kJ mol^{-1} at different pore occupancies.

	Ultramicropores	Ultramicro- and micropores		All available pores	
	QE	QE1	QE2	QE1	QE2
C700	1.37±0.12	1.45±0.15	1.54±0.11	0.05±0.15	0.04±0.10
C800	0.97±0.10	1.31±0.64	1.37±0.12	0.44±0.14	0.32±0.10
C900	0.38±0.09	0.03±0.06	1.14±0.17	0.38±0.14	0.26±0.04

It has been shown previously that the mesopores of C700 are prevalently cylindrical and with increased synthesis temperature, the shape of pores changes to more slit-shaped geometry [8]. In addition, it has been demonstrated that cylindrical geometry limits the mobility of H_2 to a larger extent than the slit-shaped geometry of the pores [9]. As the synthesis temperature increases in the series C700, C800 and C900, the volume of the ultramicropores of the sample decreases and the slit-shape geometry of the pore starts to dominate instead of the cylindrical geometry of the pores. Thus, porous structure becomes less confining for H_2 when the synthesis temperature increases. This is evidenced by the decreasing of E_a-s, i.e. the energetical barrier, which needs to be exceeded for the diffusion process to occur. The decrease in E_a with the synthesis temperature of carbon

shows that H_2 becomes less hindered, i.e. more mobile as the volume of ultramicropores decreases and the slit-shaped geometry of the pores starts to dominate.

The nature of the diffusion processes occurring in two different time scales in C700, C800 and C900 when H_2 is adsorbed in ultramicro- and micropores and all available pores cannot be accurately separated and determined with the applied fitting method, meaning that the E_a-s do not show a clear dependency on the volume of the pores nor on the pore geometry. This is attributed to the complexity of distinguishing different diffusing entities, such as H_2 monolayer adsorption, multilayer adsorption, intermolecular interactions, and accurately confirming their hindrance. The accurate resolving of two different diffusing entities will be investigated more thoroughly in the future.

The E_a values of both QE1 and QE2 adsorbed in micro- and ultramicropores are in general larger compared to the E_a values of H_2 adsorbed only in ultramicropores, showing that the presence of the micropores in addition to ultramicropores help to confine the H_2 moelcules. When H_2 is in addition to micro- and ultramicropores adsorbed in mesopores, i.e., H_2 is adsorbed in all available pores, H_2 mobility is the least hindered, indicated by the lowest E_a values, showing that mesopores additionally to micro- and ultramicropores do not have noticable effect on confining of the H_2 molecules.

C700, C800 and C900 all have lower micropore volume fractions than PFAC and UMC investigated previously in Ref.[12]. Therefore, the E_a values of H_2 adsorbed in PFAC and UMC at low H_2 loading pressures are higher than the E_a values for H_2 adsorbed in C700, C800 and C900 at low H_2 loading pressure, indicating that materials with higher micropore volume fractions hinder the mobility of H_2 to a larger extent.

Summary

The porous structure (specific surface area, pore volume and pore size distribution) of three Mo_2C derived carbon materials synthesized at 700 ºC, 800 ºC and 900 ºC (denoted as C700, C800 and C900, respectively) have been characterized with N_2, Ar, CO_2 and H_2 gas adsorption method. The diffusion of H_2 adsorbed in porous structure of the materials was investigated with quasi-elastic neutron scattering (QENS) method.

Gas adsorption measurements with different gases and at different measurement conditions enabled to accurately determine the pore size distribution of the materials, which exhibit ultramicropores (width < 7 Å), micropores (7 Å < width < 20 Å) and mesopores (20 Å < width < 500 Å). It was concluded that as the synthesis temperature increases from 700 ºC to 900 ºC, the specific surface area and pore volume of the sample decreases.

The QENS experiment was carried out at H_2 loading pressures of 68 mbar or 86 mbar (low pressure), 1 bar (moderate pressure) and 10 bar (high pressure) and at different temperatures from 50 K to 100 K. Using Hall-Ross and Singwi-Sjölander translational jump diffusion models, diffusion coefficient values (D) were calculated at different fixed temperatures. Arrhenius type equation was used to calculate the activation energy (E_a) of the diffusion process.

From the pressure readings of the sample cell, it was concluded that at 50 K and at low pressure, H_2 was adsorbed predominantly in the ultramicropores, at moderate pressure, H_2 was predominantly adsorbed in ultramicro- and micropores and at high pressure, H_2 was adsorbed in all available pores. It was seen for all pressures that as the temperature increases, the D values also increase, showing that the increase in temperature induces the faster motion and desorption of H_2 molecules. At low pressure, the small D values of H_2 adsorbed in C700 and C800 at 50 K indicates a very strong confinement of the H_2 molecules. As the ultramicropore volume decreases, H_2 becomes more mobile. At moderate and high pressure and at higher temperature range, H_2 diffusion in the two time scales is observed and this effect will be investigated more thoroughly in the future. The E_a values at different loading pressures indicate that micropores in addition to ultramicropores help to confine H_2, but mesopores additionally to micro- and ultramicropores do not have noticable effect on confining H_2 molecules.

Kokkuvõte

Kolme Mo_2C-st sünteesitud materjali (kloreerimistemperatuur 700 ºC, 800 ºC ja 900 ºC ja edasi nimetatud C700, C800 ja C900) poorset struktuuri kirjeldati N_2, Ar, CO_2 ja H_2 adsorptsiooni meetodil. Nendes materjalides adsorbeerunud H_2 difusiooni (liikuvust) uuriti kvaasi-elastse neutronhajumise (*Quasi-elastic neutron scattering*, QENS) meetodiga.

Mitme gaasiga (N_2, Ar, CO_2 ja H_2) adsorptsiooni mõõtmise eeliseks on, et nii saab usaldusväärselt kirjeldata poorset struktuuri laias poorisuuruste vahemikus. See võimaldab kirjeldada nii ultramikropoore (poori laius < 7 Å), mikropoore (7 < poori laius < 20 Å) kui ka mesopoore (poori laius > 20 Å). Leiti, et sünteesitemperatuuri suurenedes materjalide eripind ja pooriruumala vähenevad.

Kvaasielastse neutronhajumine mõõtmine viidi läbi kolmel H_2 laadimisrõhul – 68 mbar või 86 mbar (madal laadimisrõhk), 1 bar (keskmine laadimisrõhk) ja 10 bar (kõrge laadimisrõhk) ning kuuel fikseeritud temperatuuril vahemikus 50–100 K. Eksperimentaalseid tulemusi lähendati Singwi-Sjölanderi ja Hall-Rossi hüppedifusiooni mudelitega, mille põhjal leiti difusioonikoefitsiendi väärtused (D) erinevatel temperatuuridel. Difusiooniprotsessi aktivatsioonienergia (E_a) arvutamiseks lähendati tulemusi Arrheniuse-tüüpi võrrandiga.

Rõhumõõtmisandmetest järeldati, et 50 K juures madalal H_2 laadimisrõhul oli H_2 adsorbeerunud eelkõige ultramikropoorides, keskmisel laadimisrõhul oli H_2 adsorbeerunud eelkõige ultramikro- ja mikropoorides ning kõrgemal laadimisrõhul oli H_2 adsorbeerunud kõikides poorides. Tulemuseks saadi, et temperatuuri kasvades H_2 liikuvus suureneb ning H_2 desorbeerub. Madalatel temperatuuridel oli H_2 liikuvus C700 ja C800 ultramikropoorides väga piiratud. Kui ultramiktopooride ruumala väheneb, siis H_2 muutub liikuvamaks. Keskmisel ning kõrgemal rõhul ja kõrgematel temperatuuridel oli näha H_2 liikumist kahes erinevas kiiruste piirkonnas, mida uuritakse põhjalikumalt edaspidi. E_a väärtustest järeldati, et mikropoorid lisaks ultramikropooridele aitavad piirata H_2 liikuvust, aga mesopooride võimekus H_2 liikumist takistada on oluliselt väiksem.

References

[1] M. Hirscher, *Handbook of Hydrogen Storage: New Materials for Future Energy Storage*, John Wiley & Sons, **2010**.

[2] "DOE Technical Targets for Onboard Hydrogen Storage for Light-Duty Vehicles," can be found under https://www.energy.gov/eere/fuelcells/doe-technical-targets-onboard-hydrogen-storage-light-duty-vehicles, **n.d.**

[3] R. B. Gupta, *Hydrogen Fuel: Production, Transport, and Storage*, CRC Press, **2008**.

[4] J. Zheng, C.-G. Wang, H. Zhou, E. Ye, J. Xu, Z. Li, X. J. Loh, *Research* **2021**, *2021*, 1.

[5] H. Wang, Q. Gao, J. Hu, *J. Am. Chem. Soc.* **2009**, *131*, 7016.

[6] E. Masika, R. Mokaya, *J. Phys. Chem. C* **2012**, *116*, 25734.

[7] A. Jänes, T. Thomberg, H. Kurig, E. Lust, *Carbon* **2009**, *47*, 23.

[8] R. Palm, R. Härmas, E. Härk, B. Kent, H. Kurig, M. Koppel, M. Russina, I. Tallo, T. Romann, J. Mata, K. Tuul, E. Lust, *Carbon* **2021**, *171*, 695.

[9] R. Härmas, R. Palm, M. Russina, H. Kurig, V. Grzimek, E. Härk, M. Koppel, I. Tallo, M. Paalo, O. Oll, J. Embs, E. Lust, *Carbon* **2019**, *155*, 122.

[10] M. Koppel, R. Palm, R. Härmas, M. Russina, N. Matsubara, M. Månsson, V. Grzimek, M. Paalo, J. Aruväli, T. Romann, O. Oll, E. Lust, *Carbon* **2021**, *174*, 190.

[11] A. C. Dillon, M. J. Heben, *Appl Phys A* **2001**, *72*, 133.

[12] C. I. Contescu, D. Saha, N. C. Gallego, E. Mamontov, A. I. Kolesnikov, V. V. Bhat, *Carbon* **2012**, *50*, 1071.

[13] Y. Gogotsi, C. Portet, S. Osswald, J. M. Simmons, T. Yildirim, G. Laudisio, J. E. Fischer, *International Journal of Hydrogen Energy* **2009**, *34*, 6314.

[14] T. S. Blankenship Ii, N. Balahmar, R. Mokaya, *Nature Communications* **2017**, *8*, 1.

[15] J. Rouquerol, F. Rouquerol, P. Llewellyn, G. Maurin, K. S. W. Sing, *Adsorption by Powders and Porous Solids: Principles, Methodology and Applications*, Academic Press, **2013**.

[16] P. W. Atkins, J. De Paula, *Physical Chemistry*, W. H. Freeman And Co., New York, **2010**.

[17] A. L. Myers, P. A. Monson, *Adsorption* **2014**, *20*, 591.

[18] E. R. S. Winter, *Transactions of the Faraday Society* **1951**, *47*, 342.

[19] American Institute of Physics, B. H. Billings, D. E. Gray, *American Institute of Physics Handbook*, McGraw-Hill, New York, **1972**.

[20] J. Jagiello, M. Thommes, *Carbon* **2004**, *42*, 1227.

[21] D. Lässig, J. Lincke, J. Moellmer, C. Reichenbach, A. Moeller, R. Gläser, G. Kalies, K. A. Cychosz, M. Thommes, R. Staudt, H. Krautscheid, *Angewandte Chemie* **2011**, *123*, 10528.

[22] A. I. Skoulidas, D. S. Sholl, *J. Phys. Chem. B* **2005**, *109*, 15760.

[23] R. Hempelmann, *Quasielastic Neutron Scattering and Solid State Diffusion*, Clarendon Press, **2000**.

[24] M. Bee, *Quasielastic Neutron Scattering: Principles and Applications in Soild State Chemistry, Biology and Materials Science*, Adam Hilger, Bristol (UK), **1988**.

[25] V. Cristiglio, G. J. Cuello, M. Jiménez-Ruiz, in *Comprehensive Supramolecular Chemistry II* (Ed.: J.L. Atwood), Elsevier, Oxford, **2017**, pp. 263–288.

[26] R. Pynn, *Los Alamos Science* **1990**, *19*, 33.

[27] M. T. F. Telling, *A Practical Guide to Quasi-Elastic Neutron Scattering*, **2020**.

[28] "Neutron Scattering Lengths and cross sections," can be found under https://www.ncnr.nist.gov/resources/n-lengths/elements/h.html, **n.d.**

[29] M. Bée, *Chemical Physics* **2003**, *292*, 121.
[30] C. T. Chudley, R. J. Elliott, *Proc. Phys. Soc.* **1961**, *77*, 353.
[31] P. L. Hall, D. K. Ross, *Molecular Physics* **1981**, *42*, 673.
[32] K. S. Singwi, A. Sjölander, *Phys. Rev.* **1960**, *119*, 863.
[33] E. Bahn, O. Czakkel, B. Nagy, K. László, S. Villar-Rodil, J. M. D. Tascón, F. Demmel, M. T. F. Telling, P. Fouquet, *Carbon* **2016**, *98*, 572.
[34] E. Bahn, L. A. Hoyos Giraldo, V. Kuznetsov, I. Calvo-Almazán, M. Zbiri, M. M. Koza, T. C. Hansen, P. F. Henry, A. Lapp, S. Pouget, M. Mesa, P. Fouquet, *Carbon* **2020**, *166*, 307.
[35] S. Brunauer, P. H. Emmett, E. Teller, *J. Am. Chem. Soc.* **1938**, *60*, 309.
[36] J. Jagiello, C. O. Ania, J. B. Parra, L. Jagiello, J. J. Pis, *Carbon* **2007**, *45*, 1066.
[37] J. Jagiello, J. P. Olivier, *Adsorption* **2013**, *19*, 777.
[38] J. Jagiello, J. P. Olivier, *Carbon* **2013**, *55*, 70.
[39] M. Russina, G. Guenther, V. Grzimek, R. Gainov, M.-C. Schlegel, L. Drescher, T. Kaulich, W. Graf, B. Urban, A. Daske, K. Grotjahn, R. Hellhammer, G. Buchert, H. Kutz, L. Rossa, O.-P. Sauer, M. Fromme, D. Wallacher, K. Kiefer, B. Klemke, N. Grimm, S. Gerischer, N. Tsapatsaris, K. Rolfs, *Physica B: Condensed Matter* **2018**, *551*, 506.
[40] O. Arnold, J. C. Bilheux, J. M. Borreguero, A. Buts, S. I. Campbell, L. Chapon, M. Doucet, N. Draper, R. Ferraz Leal, M. A. Gigg, V. E. Lynch, A. Markvardsen, D. J. Mikkelson, R. L. Mikkelson, R. Miller, K. Palmen, P. Parker, G. Passos, T. G. Perring, P. F. Peterson, S. Ren, M. A. Reuter, A. T. Savici, J. W. Taylor, R. J. Taylor, R. Tolchenov, W. Zhou, J. Zikovsky, *Nuclear Instruments and Methods in Physics Research. Section A, Accelerators, Spectrometers, Detectors and Associated Equipment* **2014**, *764*, DOI 10.1016/j.nima.2014.07.029.
[41] M. Angst, Forschungszentrum Jülich, Jülich Centre for Neutron Science, *Scattering Methods for Condensed Matter Research: Towards Novel Applications at Future Sources*, **2012**.
[42] S. Mascotto, D. Kuzmicz, D. Wallacher, M. Siebenbürger, D. Clemens, S. Risse, J. Yuan, M. Antonietti, M. Ballauff, *Carbon* **2015**, *82*, 425.
[43] B. Schmitz, U. Müller, N. Trukhan, M. Schubert, G. Férey, M. Hirscher, *ChemPhysChem* **2008**, *9*, 2181.
[44] D. D. Do, *Adsorption Analysis: Equilibria and Kinetics*, Imperial College Press, London, **1998**.
[45] "Thermophysical Properties of Fluid Systems," can be found under https://webbook.nist.gov/chemistry/fluid/, **n.d.**

Acknowledgements

I would like to thank Riinu Härmas and Rasmus Palm for supervision; Maarja Paalo and Indrek Tallo for synthesizing the samples; Ove Oll, Heisi Kurig and Veronika Grzimek for co-conducting the QENS measurements and Jacek Jagiello for modeling pore size distributions of the samples. I would also like to thank the Chair of Physical Chemistry and prof. Enn Lust.

I would like to express my gratitude towards Helmoltz Zentrum Berlin for the QENS measurement and Estonian Ministry of Education and Research for funding the research through SLTKT16432T "Estonian participation in designing, construction and application of the ESS 1.09.2015-31.08.2023)".

Appendix A. Calculating the ratio of filled pores

Sips equation (Equation A1) was applied to calculate the amount of adsorbed H_2 (n_{ads}) [44].

$$n_{ads} = n_{ads}^{max} \frac{(Kp)^{1/n}}{1 + (Kp)^{1/n}} \quad \text{(A1)}$$

where n_{ads} is the amount of adsorbed gas, n_{ads}^{max} is the amount of adsorbed gas at full surface coverage, K is equilibrium coefficient, p is the adsorbate's partial pressure and n is heterogeneity coefficient.

Isotherms measured with H_2 at 77 K for C700, C800 and C900 were fitted with Sips equation was (Figure A1).

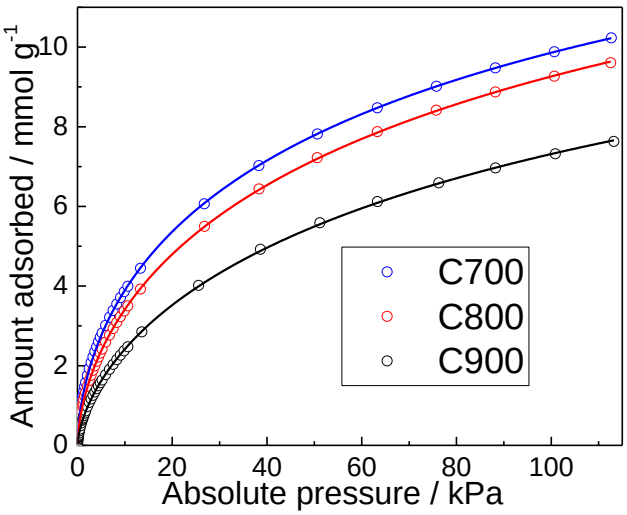

Figure A1. C700, C800 and C900 (noted in the graph) H_2 isotherms fitted with Sips equation.

The resulting (n_{ads}^{max}, K and n) obtained from fitting the Sips equation are presented in Table A1.

Table A1. Amount of adsorbed gas at full surface coverage (n_{ads}^{max}), equilibrium coefficient *(K)* and heterogeneity parameter (*n*) obtained from fitting Sips equation with C700, C800 and C900 H_2 isotherms.

	n_{ads}^{max} / mmol g^{-1}	K / kPa^{-1}	n / unitless
C700	20.62	0.0086	1.68
C800	20.91	0.0069	1.64
C900	17.29	0.0062	1.53

For calculating n_{H2}, the free volume of the sample holder (V_f = 0.0241 dm^3), H_2 density at 77 K (ρ), the amount of not adsorbed H_2 ($n_{H2,f}$) and the mass of the sample (m_{700} = 0.35 g, m_{800} = 0.314 g and m_{900} = 0.3541 g) were taken into account. H_2 densities at different pressures at 77 K were obtained from the NIST database [45]. To calculate n_{H2}, Equation A2 was used and the results are presented in Table A2.

$$n_{H2} = \frac{n_{H2,f} + n_{ads}}{m_x} \quad \text{(A2)}$$

where $n_{H2,f} = 1000 V_f \rho$ and the subscript x in m_x denotes the chlorination temperature of the CDCs.

Table A2. The calculated total amounts of H_2 in the sample holder per sample mass (n_{H2}).

	C700			**C800**			**C900**		
p_{H2} (kPa)	6.8	100	1000	8.6	100	1000	8.6	100	1000
n_{ads} (mmol)	1.13	3.45	5.65	0.99	2.91	5.02	0.79	2.59	4.70
ρ (mol dm^{-3})	0.011	0.16	1.59	0.013	0.16	1.59	0.013	0.16	1.59
$n_{H2,f}$ (mmol)	0.26	3.77	38.24	0.32	3.77	38.24	0.32	3.77	38.24
n_{H2} (mmol g^{-1})	4	21	125	4	21	138	3	18	121

n_{ads} is calculated according to Sips equation (Equation A1) and p_{H2} denotes the loading pressure of H_2.

Onward there are calculations only for C700 at 68 mbar because the calculation procedure is similar to C800 and C900 over the pressure range. To calculate the ratio of filled pores (F), firstly, the amount of H_2 adsorbed in the porous structure of the samples at different temperatures and different amounts of H_2 in the sample holder (n_c) (Table A2) were calculated. Considering the pressure in the sample holder (p_{SH}, Table A3), the temperature difference in different volumes of the sample holder (V_{300} = 0.012 dm^3 and V_c = 0.011 dm^3 stand for the volume of the samples holder's warm and cold part), H_2 density at different temperatures and pressures (ρ_{H2}) and T = 300 K and different pressures (ρ_{300}), the amount of H_2 per sample (n_c) were calculated as follows:

$$n_C = n_{H2} - \frac{\rho_{300} V_{300}}{m_{700}} - \frac{\rho_{H2} V_c}{m_{700}} \quad \text{(A3)}$$

n_{H2} - total amount of H_2 in the sample holder per sample mass; ρ_{300} – H_2 density at T = 300 K; V_{300} – volume of the sample holder's warm part; ρ_{H2} – H_2 density at different temperatures and pressures; V_c – volume of the sample holder's cold part; m_{700} – C700-s mass.

Table A3. Pressure readings (p_{SH}) in the sample cell (bar) during the measurement.

Sample	C700			C800			C900		
p_{H2} / bar T / K	0.068	1	10	0.086	1	10	0.086	1	10
50	5.22E-4	0.085	6.16	8.34E-4	0.099	6.01	0.0023	0.40	7.26
60	0.0054	0.33	7.80	0.0087	0.37	7.77	0.015	0.62	8.67
70	0.029	0.72	9.30	0.040	0.76	9.11	0.049	0.88	9.96
80	0.089	1.20	10.79	0.11	1.20	10.42	0.11	1.13	11.12
90	0.19	1.68	12.20	0.21	1.64	11.63	0.16	1.39	--*
100	0.30	2.15	13.53	0.32	2.05	12.76	0.21	1.61	--*

*The equilibrium pressure could not be reliably measured for C900 at 10 bar at 90 K and 100 K.

To calculate the ratio of all filled pores (F_{tot}) and filled ultramicropores (F_{ump}), it was assumed that the adsorbed H_2 has the density of liquid H_2. F_{tot} and F_{ump} were calculated from the n_c, the density of liquid H_2 (ρ_L = 35.17 mol dm^{-3}) the pore volume (V_{tot} = 1.76 cm^3 g^{-1}), ultramicropore volume (V_{ump} = 0.012 cm^3 g^{-1}) and combined micro- and ultramicropore volume according to Equation A4 and A5. The results are presented in Table A4.

$$F_{tot} = \frac{n_c}{V_{tot}\rho_L}\ 100\ \% \qquad \text{(A4)}$$

$$F_{ump} = \frac{n_c}{V_{ump}\rho_L}\ 100\ \% \qquad \text{(A5)}$$

Tabel A4. The amount of H_2 adsorbed in the porous structure (n_c) of , the ratios of all filled pores (F_{tot}) and filled ultramicropores (F_{ump}) of C700.

p_{SH} / mbar	ρ_{300} / mmol dm^{-3}	T / K	ρ_{H2} / mmol dm^{-3}	n_c / mmol g^{-1}	F_{tot} / %	F_{ump} / %
0.52	0.02	50	0.13	3.95	6	90
5.42	0.22	60	1.09	3.91	6	90
29.07	1.17	70	5.00	3.75	6	90
89.20	3.58	80	13.41	3.39	5	80
186.09	7.46	90	24.87	2.88	4	70
304.21	12.19	100	36.59	2.35	3	60

The ratio of all filled pores (F_{tot}), filled ultramicropores (F_{ump}) and filled micro- and ultramicropores (F_{u+m}) at other pressures for all the materials are presented in table A5.

Tabel A5. The ratio of all filled pores (F_{tot}), filled ultramicropores (F_{ump}) and filled micro- and ultramicropores (F_{u+m}) in % at different pressures (p_{H2}) and temperatures for all the materials.

p_{H2} / bar	0.086				1						10		
Sample	C800		C900		C700		C800		C900		C700	C800	C900
F / % T / K	F_{tot}	F_{ump}	F_{tot}	F_{ump}	F_{tot}	F_{u+m}	F_{tot}	F_{u+m}	F_{tot}	F_{u+m}	F_{tot}	F_{tot}	F_{tot}
50	7	100*	6	100*	30	90	40	100*	30	100*	100*	100*	100
60	7	100*	6	100*	30	80	30	100*	30	100*	100	100*	100
70	7	100*	6	100*	30	70	30	100	20	100	90	100*	100
80	6	100*	5	100	20	60	20	90	20	100	90	100*	100
90	5	100	4	90	20	50	20	70	20	90	90	100*	--
100	4	80	4	80	20	40	20	60	20	80	90	100*	--

The ratios could not be calculated for C900 at 10 bar at 90 K and 100 K because the equilibrium pressure could not be reliably measured.

100* - pores were filled <100%, indicating than when 7% and 30% of the pores were filled, some of the H_2 was already in micropores and mesopores, respectively.

Appendix B. Some reduced chi-squared values

Reduced chi-square is a statistical measure which is used to test whether any given data are well described by some hypothesized function. It can be used to determine whether a model with one or two Lorentzian functions is more sufficient to describe the experimental data. In general, reduced chi-squared value near 1 is an indication of a good fit, but if the value is too small, the model is overfitting the data. Reduced chi-squared value significantly larger than 1 indicates that the model fits poorly the experimental data.

Table B1. Some reduced chi-squared values for C700-s H_2 spectra. The trends were analogue with C800 and C900 H_2 spectra over the temperatures.

Filled pores	Ultra-micropores	Micro- and ultramicropores				All available pores			
T / K	60	60		70		50		100	
Model / Q / Å^{-1}	L	L1	L2	L1	L2	L1	L2	L1	L2
0.725	1.1	4.9	0.9	4.9	1.0	25.9	2.9	13.1	3.6
0.875	1.1	5.4	0.7	5.9	0.9	16.7	1.2	10.2	4.1
1.025	1.1	4.7	0.6	5.5	0.9	9.5	1.1	8.4	4.6
1.175	1.2	4.3	0.7	5.5	1.2	6.7	1.4	9.5	5.7

Appendix C. Selection of quasi-elastic (QE, QE1 and QE2) and elastic (EL) component fractions in total signal

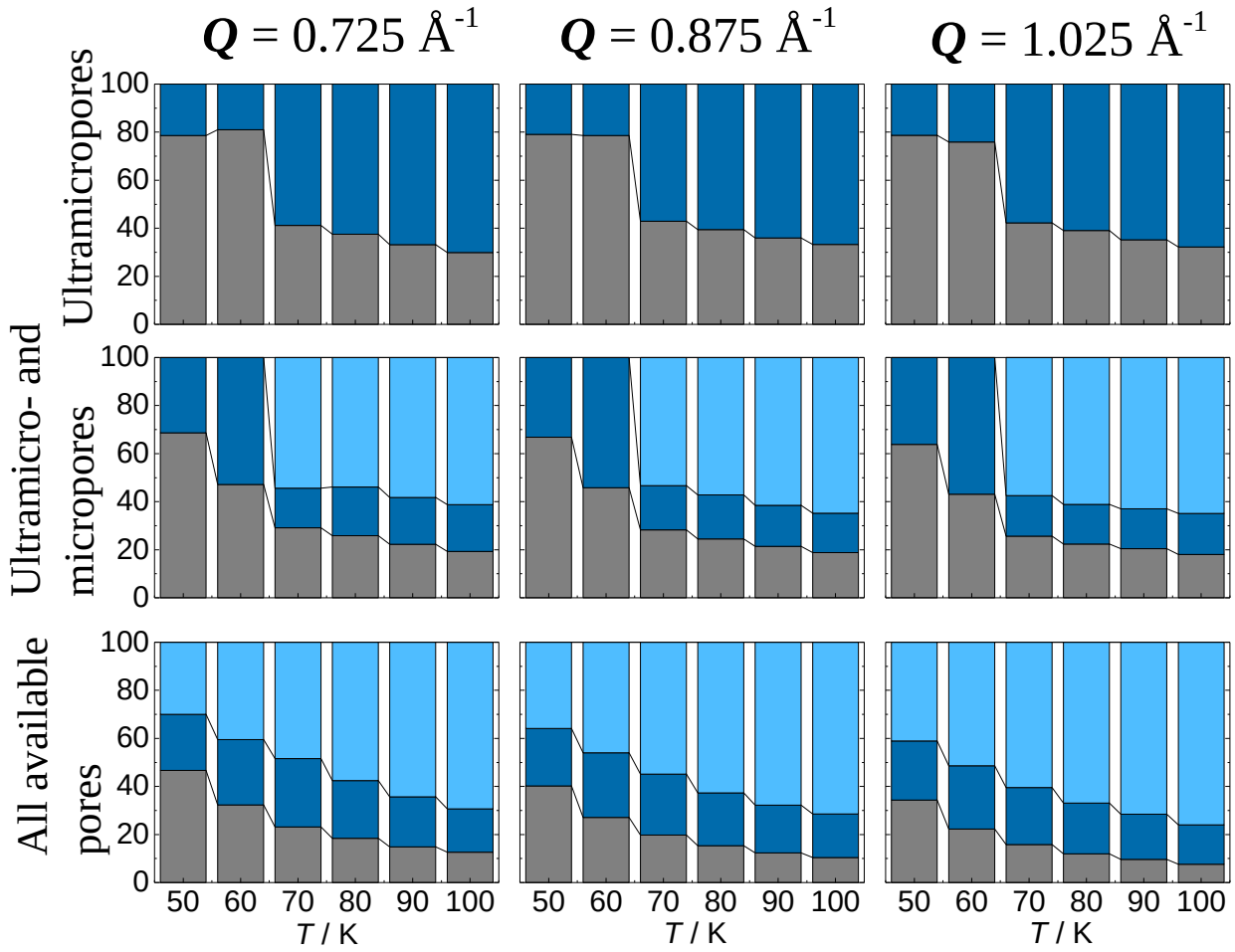

Figure C1. Narrow and broad QE component (dark and light blue, respectively) and EL component (gray) fractions in total signal of the C700-s H_2 spectra at Q = 0.775 Å^{-1}, Q = 0.875 Å^{-1} and Q = 1.025 Å^{-1} when H_2 is adsorbed only in ultramicropores, ultramicro-and micropores and all available pores. The sum of the components is unity, e.i. $A_0 + \sum_{i=1}^{n} A_i = 1$, where n denotes the number of QE components.

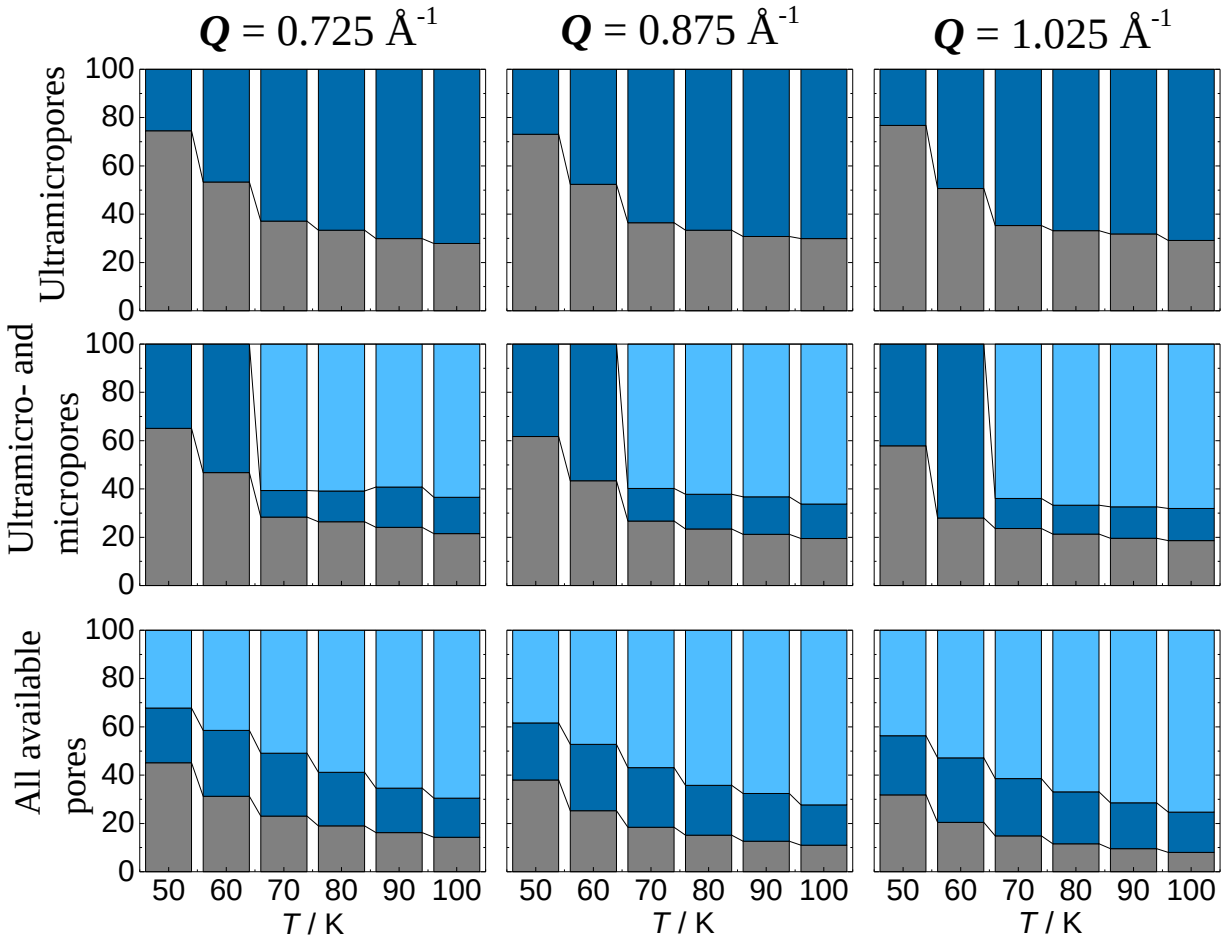

Figure C2. Narrow and broad QE component (dark and light blue, respectively) and EL component (gray) fractions in total signal of the C800-s H_2 spectra at Q = 0.775 Å^{-1}, Q = 0.875 Å^{-1} and Q = 1.025 Å^{-1} when H_2 is adsorbed only in ultramicropores, ultramicro-and micropores and all available pores. The sum of the components is unity, i.e. $A_0 + \sum_{i=1}^{n} A_i = 1$, where n denotes the number of QE components.

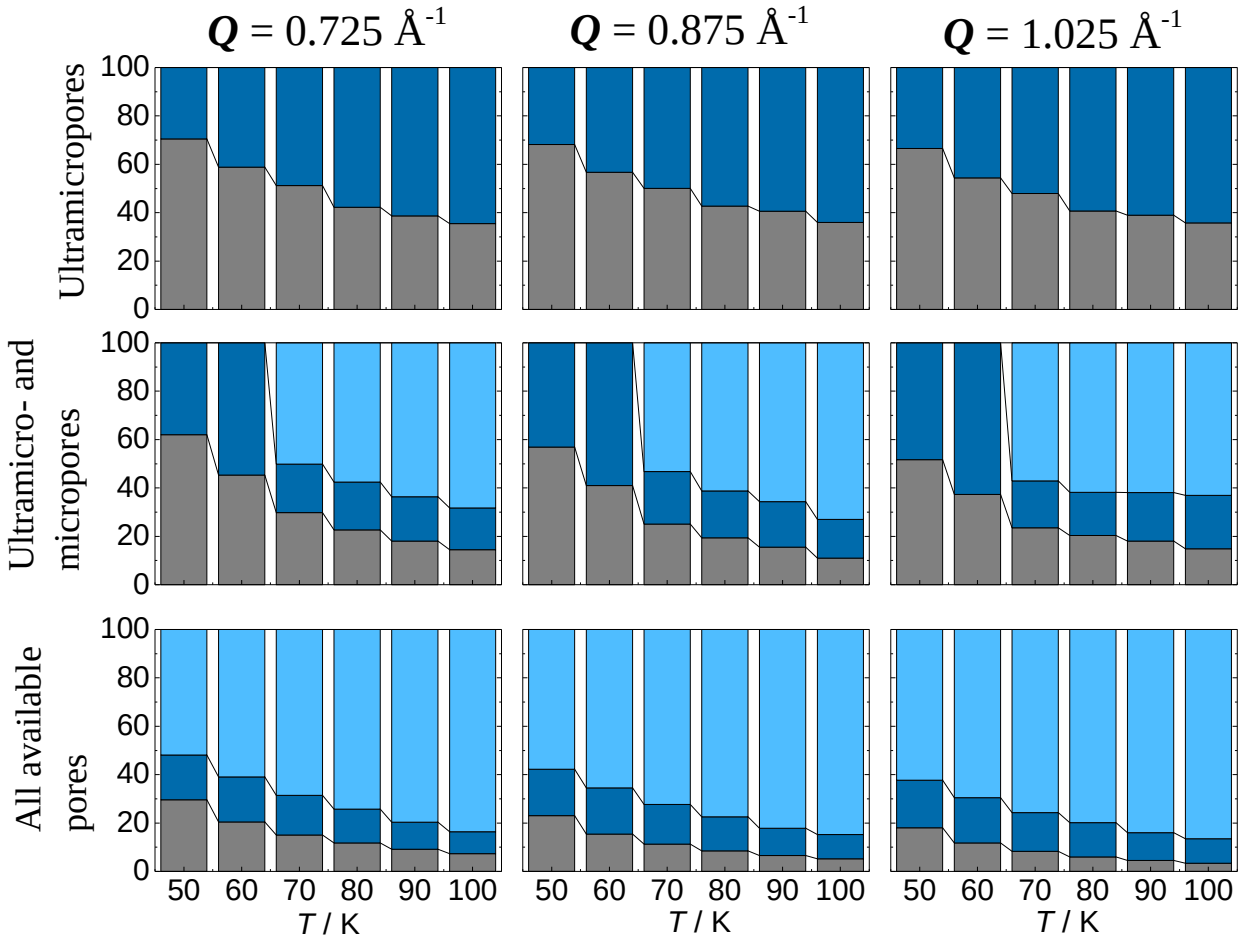

Figure C3. Narrow and broad QE component (dark and light blue, respectively) and EL component (gray) fractions in total signal of the C900-s H_2 spectra at Q = 0.775 Å^{-1}, Q = 0.875 Å^{-1} and Q = 1.025 Å^{-1} when H_2 is adsorbed only in ultramicropores, ultramicro-and micropores and all available pores. The sum of the components is unity, i.e. $A_0 + \sum_{i=1}^{n} A_i = 1$, where n denotes the number of QE components.

Appendix D. 2D-NLDFT-HS experimental results and model fits

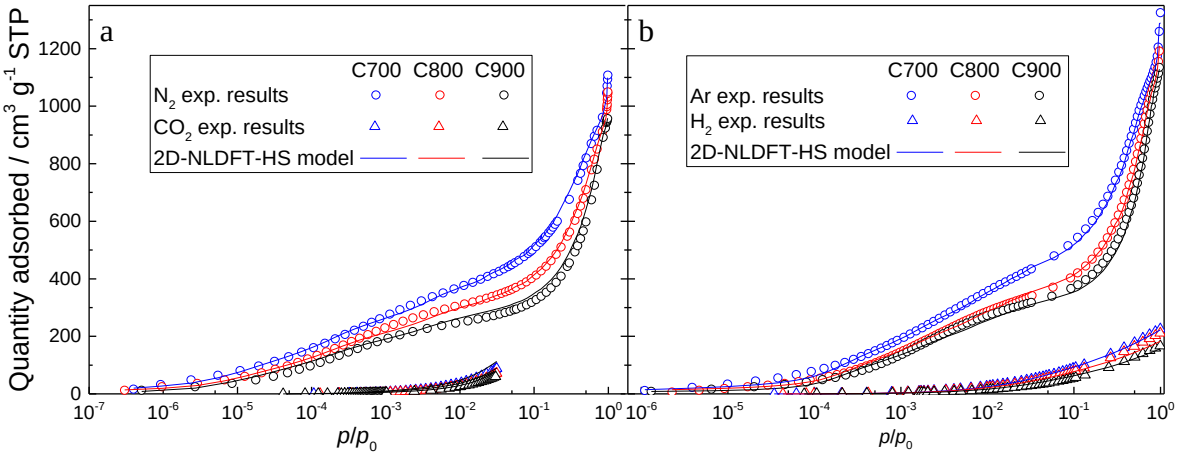

Figure D1. Experimental adsorption isotherms of C700, C800 and C900 measured with N_2 (a), Ar (b), CO_2 (a) and H_2 (b) and their corresponding 2D-NLDFT-HS model fitting results.

Appendix E. Diffusion coefficients of H_2 ($Å^2\ ps^{-1}$) in C700, C800 and C900 at different pore occupancies and at different temperatures

Filled pores	Ultramicropores			Ultramicro- and micropores						All available pores					
	QE			QE1			QE2			QE1			QE2		
Sample	C700	C800	C900	C700	C800	C900	C700	C800	C900	C700	C800	C900	C700	C800	C900
50 K	0.36± 0.02	0.17± 0.01	2.69± 0.06	1.14± 0.05*	1.20± 0.06*	1.47± 0.08*				0.32± 0.02	0.34± 0.02	0.33± 0.02	3.56± 0.25	3.31± 0.19	3.38± 0.24
60 K	2.42± 0.07	2.74± 0.14	3.19± 0.07	1.77± 0.09*	1.72± 0.08*	2.26± 0.14*				0.58± 0.03	0.62± 0.02	0.46± 0.03	3.13± 0.15	3.31± 0.18	3.47± 0.29
70 K	4.15± 0.11	3.50± 0.10	3.98± 0.19	0.47± 0.08	0.43± 0.08	1.03± 0.15	1.58± 0.07	1.53± 0.06	3.56± 0.35	0.89± 0.07	0.76± 0.05	0.53± 0.03	2.73± 0.13	2.60± 0.09	3.68± 0.35
80 K	5.42± 0.15	4.81± 0.12	3.86± 0.08	0.64± 0.08	0.43± 0.11	1.07± 0.11	2.32± 0.08	2.22± 0.11	5.16± 0.48	0.81± 0.07	0.76± 0.05	0.60± 0.03	2.56± 0.11	2.61± 0.17	4.01± 0.41
90 K	6.12± 0.16	5.52± 0.12	4.08± 0.21	0.88± 0.18	0.86± 0.21	1.03± 0.11	2.99± 0.17	2.71± 0.12	5.49± 0.48	0.88± 0.06	0.86± 0.06	0.58± 0.03	2.68± 0.23	2.81± 0.18	4.11± 0.35
100 K	7.57± 0.20	6.59± 0.18	4.58± 0.25	0.96± 0.17	0.73± 0.11	1.06± 0.13	3.45± 0.22	3.10± 0.16	6.62± 0.98	0.89± 0.09	0.94± 0.09	0.67± 0.06		3.03± 0.17	4.25± 0.63

*Calculated from one-Lorentzian model fitting results

Appendix F. Mean jump lengths of H_2 (Å) in C700, C800 and C900 at different pore occupancies and at different temperatures

Filled pores	Ultramicropores			Ultramicro- and micropores						All available pores					
	QE			QE1			QE2			QE1			QE2		
Sample	C700	C800	C900	C700	C800	C900	C700	C800	C900	C700	C800	C900	C700	C800	C900
50 K	2.47± 0.15	1.33± 0.03	5.52± 0.07	2.81± 0.10*	2.70± 0.11*	2.93± 0.13*				1.44± 0.10	1.39± 0.10	1.18± 0.16	1.68± 0.16	1.56± 0.13	1.54± 0.15
60 K	4.37± 0.07	5.17± 0.12	5.94± 0.07	3.10± 0.13*	2.81± 0.12*	3.34± 0.16*				2.01± 0.11	1.95± 0.07	1.25± 0.15	1.57± 0.11	1.68± 0.12	1.43± 0.21
70 K	5.47± 0.09	4.71± 0.09	6.52± 0.17	2.30± 0.33	2.18± 0.39	3.20± 0.33	1.52± 0.13	1.47± 0.11	2.91± 0.39	2.53± 0.16	1.91± 0.14	1.28± 0.11	1.42± 0.11	1.36± 0.09	1.48± 0.25
80 K	6.22± 0.10	5.55± 0.08	6.20± 0.07	2.63± 0.29	1.88± 0.55	3.12± 0.25	2.04± 0.10	1.97± 0.13	3.76± 0.52	2.03± 0.19	1.64± 0.14	1.26± 0.12	0.88± 0.15	1.05± 0.21	1.55± 0.29
90 K	6.33± 0.10	5.75± 0.07	6.26± 0.18	3.16± 0.48	2.83± 0.55	2.79± 0.25	2.36± 0.15	2.04± 0.13	3.05± 0.38	2.01± 0.16	1.68± 0.15	1.02± 0.13	0.67± 0.42	0.90± 0.27	1.45± 0.26
100 K	7.57± 0.20	6.03± 0.09	6.53± 0.19	3.07± 0.42	2.24± 0.35	3.67± 0.29	2.37± 0.17	2.11± 0.16	3.67± 0.87	1.86± 0.21	1.72± 0.20	1.06± 0.22		0.81± 0.27	1.38± 0.49

*Calculated from one-Lorentzian model fitting results

Appendix G. Residence times of H_2 (ps) in C700, C800 and C900 and different pore occupancies and at different temperatures

Filled pores	Ultramicropores			Ultramicro- and micropores						All available pores					
	QE			QE1			QE2			QE1			QE2		
Sample	C700	C800	C900	C700	C800	C900	C700	C800	C900	C700	C800	C900	C700	C800	C900
50 K	2.79± 0.20	1.51± 0.02	1.89± 0.01	1.16± 0.03*	1.01± 0.04*	0.97± 0.04*				1.09± 0.10	0.95± 0.09	0.70± 0.14	0.13± 0.02	0.12± 0.01	0.12± 0.02
60 K	1.32± 0.01	1.45± 0.02	1.85± 0.01	0.90± 0.03*	0.77± 0.03*	0.82± 0.03*				1.16± 0.07	1.01± 0.04	0.57± 0.10	0.13± 0.01	0.14± 0.01	0.10± 0.02
70 K	1.20± 0.01	1.05± 0.02	1.78± 0.01	1.87± 0.24	1.82± 0.31	1.66± 0.11	0.24± 0.03	0.24± 0.03	0.35± 0.04	1.19± 0.07	0.80± 0.06	0.51± 0.06	0.12± 0.01	0.12± 0.01	0.10± 0.02
80 K	1.19± 0.01	1.07± 0.01	1.66± 0.01	1.81± 0.18	1.37± 0.45	1.52± 0.08	0.30± 0.02	0.29± 0.03	0.37± 0.04	0.85± 0.09	0.59± 0.07	0.44± 0.06	0.05± 0.02	0.07± 0.02	0.10± 0.03
90 K	1.09± 0.01	1.00± 0.01	1.60± 0.01	1.88± 0.20	1.55± 0.24	1.27± 0.09	0.31± 0.02	0.26± 0.02	0.27± 0.03	0.77± 0.07	0.55± 0.06	0.30± 0.06	0.03± 0.03	0.05± 0.03	0.09± 0.02
100 K	1.01± 0.01	0.92± 0.01	1.55± 0.01	1.63± 0.16	1.15± 0.18	1.12± 0.10	0.27± 0.02	0.24± 0.02	0.27± 0.05	0.65± 0.08	0.53± 0.07	0.29± 0.09		0.04± 0.02	0.07± 0.04

*Calculated from one-Lorentzian model fitting results

Appendix H. Singwi-Sjölander jump diffusion model fitting results

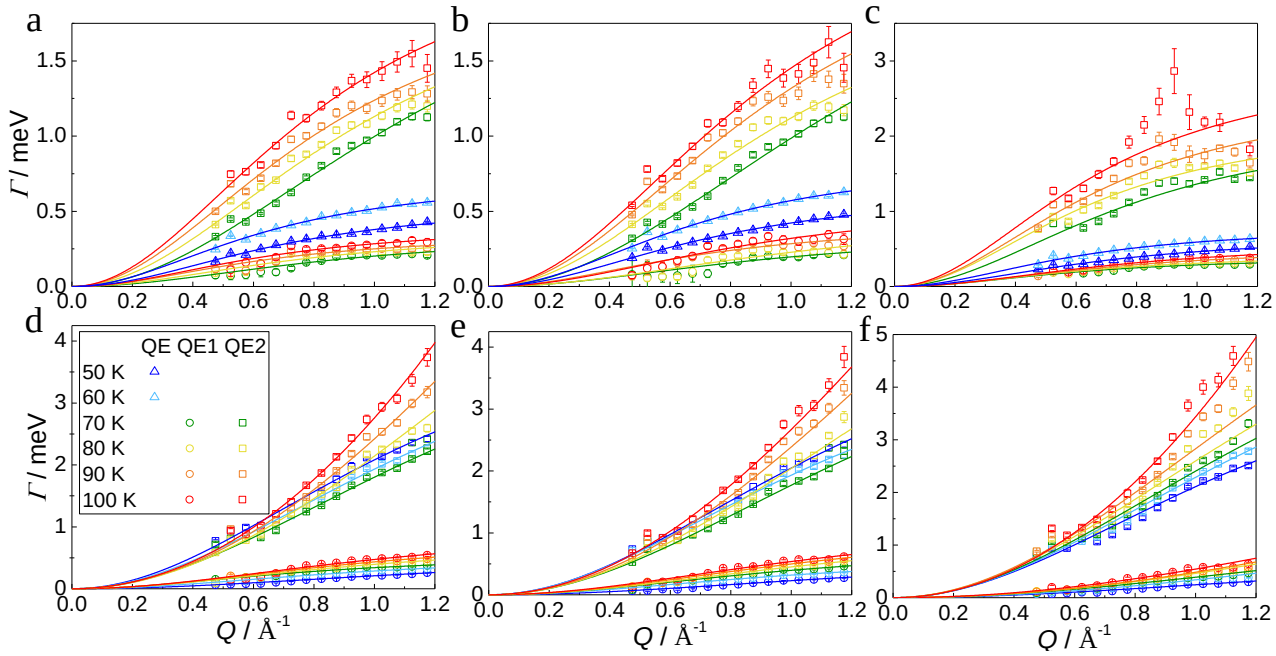

Figure H2. Variation of Γ-s (HWHM-s) obtained from fitting one-Lorentzian model (Equation 17) or two-Lorentzian model (Equation 18) over Q-values when H_2 is adsorbed in the micro- and ultramicropores of C700 (a), C800 (b) and C900 (c); when H_2 is adsorbed in all available pores of C700 (d), C800 (e) and C900 (f).

Appendix I. Maximal diffusion coefficients ($m^2\ s^{-1}\ 10^{-7}$) of H_2 at different pore occupancies

	Ultramicropores	Ultramicro- and micropores		All available pores	
	QE	QE1	QE2	QE1	QE2
C700	4.03±0.76	0.57±0.13	2.27±0.36	0.09±0.02	0.29±0.04
C800	2.04±0.34	0.39±0.36	1.67±0.29	0.16±0.03	0.44±0.06
C900	0.71±0.11	0.11±0.01	2.60±0.65	0.10±0.02	0.59±0.03

Non-exclusive licence to reproduce thesis and make thesis public

I, Miriam Koppel,
(*author's name*)

1. herewith grant the University of Tartu a free permit (non-exclusive licence) to:

1.1. reproduce, for the purpose of preservation, including for adding to the DSpace digital archives until the expiry of the term of copyright, and

1.2. make available to the public via the web environment of the University of Tartu, including via the DSpace digital archives, under the Creative Commons licence CC BY NC ND 3.0, which allows, by giving appropriate credit to the author, to reproduce, distribute the work and communicate it to the public, and prohibits the creation of derivative works and any commercial use of the work from ***4.06.2022*** until the expiry of the term of copyright,

The mobility of H_2 Adsorbed in Mo_2C Derived Carbon Materials with Different Porous Structures Studied with Quasi-Elastic Neutron Scattering,
(*title of thesis*)

supervised by Riinu Härmas and Rasmus Palm,
(*supervisor's name*)

2. I am aware of the fact that the author retains the rights specified in p. 1.

3. I certify that granting the non-exclusive licence does not infringe other persons' intellectual property rights or rights arising from the personal data protection legislation.

Miriam Koppel
4.06.2021